

1 ***Surface energy and mass balance of Mera Glacier (Nepal, Central Himalaya) and their sensitivity to***
2 ***temperature and precipitation***

3 Arbindra Khadka^{1,2,3}, Fanny Brun¹, Patrick Wagnon¹, Dibas Shrestha³, Tenzing Chogyal Sherpa²

4

5 **Affiliations**

6 ¹*University Grenoble Alpes, CNRS, IRD, IGE, Grenoble, France*

7 ²*International Centre for Integrated Mountain Development, Kathmandu, Nepal*

8 ³*Central Department of Hydrology and Meteorology, Tribhuvan University, Kirtipur, Nepal*

9

10 **This manuscript has been submitted for publication in the *Journal of Glaciology*. The manuscript**
11 **has been accepted for publication in May 2024. The published version might slightly differ, due**
12 **to the copy-editing process.**

13

14 **Abstract**

15 The sensitivity of glacier mass balance to temperature and precipitation variations is crucial for informing
16 models that simulate glaciers' response to climate change. In this study, we simulate the glacier-wide mass
17 balance of Mera Glacier with a surface energy balance model, driven by in-situ meteorological data, from
18 2016 to 2020. The analysis of the share of the energy fluxes of the glacier shows the radiative fluxes
19 account for almost all the energy available during the melt season (May to October). However, turbulent
20 fluxes are significant outside the monsoon (June to September). On an annual scale, melt is the dominant
21 mass flux at all elevations, but 44 % of the melt refreezes across the glacier. By reshuffling the available
22 observations, we create 180 synthetic series of hourly meteorological forcings to force the model over a
23 wide range of plausible climate conditions. A +1 (-1)°C change in temperature results in a -0.75 ± 0.17
24 $(+0.93 \pm 0.18)$ m w.e. change in glacier-wide mass balance and a +20 (-20)% change in precipitation results
25 in a $+0.52 \pm 0.10$ (-0.60 ± 0.11) m w.e. change. Our study highlights the need for physically based
26 approaches to produce consistent forcing datasets, and calls for more meteorological and glaciological
27 measurements in High Mountain Asia.

28 **1. INTRODUCTION**

29 The pace of climate warming in High Mountain Asia (HMA) is accelerating (Pepin and others, 2015) and
30 precipitation in these regions exhibits significant heterogeneity and remains insufficiently comprehended
31 (Lutz and others, 2014). Furthermore, the intricate relationship between precipitation and temperature
32 variations proves to be a formidable puzzle. This connection, intricately intertwined with glacier mass
33 balance, poses a challenge for understanding the recent evolution of glaciers in HMA (Oerlemans and
34 Reichert, 2000). While multi-year satellite-based estimates of mass changes allow to map the
35 heterogeneity of glacier mass balance across large scales (e.g., Hugonnet and others, 2021), they need to
36 be complemented by other approaches to further elucidate these patterns of contrasted mass losses. One
37 possible approach is to consider that glacier mass changes are the combination of a change in climate
38 conditions modulated by a glacier sensitivity to these changes (e.g., Oerlemans and Reichert, 2000;
39 Marzeion and others, 2012). Following this approach, Sakai and Fujita (2017) demonstrated that regionally
40 different sensitivity to temperature changes could be the main driver of observed mass losses across Asia.
41 They found that the glacier mass balance sensitivity to temperature was determined by the general
42 climatology, and in particular, by the summer temperature, the annual range of temperature and the ratio
43 between summer and annual precipitation. However, their approach relies on a number of simplifying

44 assumptions that consider only the climate at the equilibrium line altitude (Ohmura and others, 1992) and
45 the climate data they used has a coarse spatial resolution. There is thus room to improve the methodology
46 they applied, in particular through a better representation of processes responsible for glacier mass losses
47 and gains.

48 These processes controlling the glacier mass are determined by the surface energy balance (SEB), which is
49 commonly modelled to investigate how glacial mass balance is governed and how sensitive it is to climatic
50 variables (Fujita, 2008; Azam and others, 2014; Fugger and others, 2022). There is a long history of studies
51 that investigated the glacier SEB at various locations and at various temporal and spatial scales to relate
52 atmospheric variables to glacier mass changes (e.g., Oerlemans and Knap, 1998; Favier and others, 2004).
53 Specifically, in Hindu Kush Himalaya (HKH), a number of studies investigated the SEB of glaciers in different
54 climate contexts (Mölg and others, 2012; Zhu and others, 2015, 2018, 2021; Huintjes and others, 2015;
55 Fugger and others, 2022; Arndt and Schneider, 2023). They highlight the different sensitivities to
56 temperature and precipitation in different climate conditions, with the dry and cold (continental) climate
57 that prevails in the north west margin of HKH being associated to low sensitivities of glacier mass balance
58 to temperature, and the warmer and wetter (oceanic) climate of south east HKH corresponding to larger
59 sensitivities (e.g., Arndt and Schneider, 2023). The larger sensitivities are associated to the prevalence of
60 surface melt in the surface mass balance. Surface energy based studies find highly non linear sensitivity of
61 the mass balance to precipitation, unlike studies based on empirical approaches, such as degree-day
62 modeling (e.g., Wang and others, 2019). This is due to the highly non linear response of glacier surface
63 mass balance to the albedo effect (e.g., Arndt and Schneider, 2023).

64 However, in HKH most of the SEB studies have two main limitations: either they were done at point scale
65 (Kayastha and others, 1999; Azam and others, 2014; Acharya and Kayastha, 2019; Litt and others, 2019;
66 Mandal and others, 2022), or they used meteorological data from reanalysis products (Arndt and
67 Schneider, 2023). The point-scale modelling of the SEB is limited because the SEB is very sensitive to the
68 surface state of the glacier (ice, snow or debris), and to the distribution of meteorological variables
69 (precipitation, temperature, radiative fluxes, etc.) that vary across the glacier area (Oerlemans and others,
70 1999). Modelling the SEB of a glacier across its entire area requires distributed measurements of
71 meteorological variables, and measurements of the glacier surface mass balance at multiple locations,
72 including the accumulation area. Unfortunately, such data are seldom available in HKH (Huintjes and
73 others, 2015; Arndt and others, 2021; Srivastava and Azam, 2022; Oulkar and others, 2022).
74 Meteorological variables obtained from reanalysis can be heavily biased, especially if they are not

75 downscaled with local measurements (e.g., Hamm and others, 2020; Khadka and others, 2022). When
76 meteorological variables from reanalysis are used to force a glacier mass balance model, they first need to
77 be debiased, which is often done by tuning a precipitation correction factor until the glacier mass balance
78 matches observations. While there is usually no alternative, this method is known to be subject of
79 equifinality (e.g., Rounce and others, 2020).

80 This article presents a glacier-wide SEB analysis of Mera Glacier in the eastern part of Central Himalaya.
81 We applied the 'COupled Snowpack and Ice surface energy and mass balance model in PYthon' (COSIPY:
82 Sauter and others, 2020) which has been optimised and evaluated using site specific measurements (Fig.
83 S1 in supplementary material). Among Nepal's monitored glaciers, Mera Glacier stands out for its extensive
84 and continuous meteorological and mass balance data, making it one of the most comprehensively
85 observed glaciers in the region (Wagnon and others, 2021; Khadka and others, 2022). By integrating field
86 measurements, in-situ meteorological data, and the SEB model, we aim to enhance our understanding of
87 (1) the physical processes governing the seasonal and spatial variability of the glacier mass balance, and
88 (2) the sensitivity of the mass balance to meteorological variables. The findings from this comprehensive
89 study will give us a better understanding of the impact of the on-going climate change on Himalayan
90 glaciers.

91 **2. STUDY AREA AND CLIMATE**

92 **2.1 Mera Glacier**

93 Mera Glacier, situated in the eastern part of the Central Himalaya within the Upper Dudh Koshi basin, is a
94 plateau-type debris free glacier. Encompassing an area of 4.84 km² in 2018, the glacier stretches from an
95 altitude of 6390 m a.s.l. to a minimum of 4910 m a.s.l. (Fig. 1). This north-facing glacier features a gentle
96 slope with a mean inclination of around 16 degrees. At an elevation of approximately 5900 m a.s.l., the
97 glacier separates into two distinct branches, the Mera branch and the Naulek branch. The Mera branch
98 initially heads north and then curves westward, while the Naulek branch extends ~2 km towards the
99 northeast. The Mera branch is the largest of the two branches and accounts for about 80 % of the glacier's
100 total area.

101 "Figure 1 near here"

102 **2.2 Climate**

103 Like other glaciers in Nepal, Mera Glacier is a summer accumulation type glacier, gaining mass mainly from
104 the summer monsoon (June to September) snowfalls brought by the South Asian monsoon system
105 (Wagnon and others, 2013; Thakuri and others, 2014; Shea and others, 2015). The glacier experiences
106 most of its accumulation and ablation during the monsoon, which makes it a key season to understand the
107 climatic regime of the glacier (Ageta and Higuchi, 1984). From June to September, the average air
108 temperature measured between 2012 and 2020 at 5360 m a.s.l. on Naulek branch is 0.3 °C, and the
109 average precipitation recorded at 4888 m a.s.l. is equal to 570 mm, with an annual precipitation of 818
110 mm (Khadka and others, 2022). During this season, warm air masses flow from the Bay of Bengal and bring
111 moisture and precipitation in the Himalaya (Perry and others, 2020). In just a few days, marking the start
112 of the post-monsoon (October-November), generally at the beginning of October, meteorological
113 conditions change abruptly to become dry, sunny and increasingly cold and windy. Very occasionally, this
114 season is marked by the intrusion of typhoons in the Himalaya, which bring large amounts of snowfalls
115 above ~4000 m a.s.l. in just a few days, like in October 2013 and 2014 (Shea and others, 2015). The winter
116 (December-February) is similar but harsher than the post-monsoon with constantly cold, dry, and very
117 windy conditions. At Naulek (5360 m a.s.l.), the average air temperature during this season is -10.4 °C. The
118 pre-monsoon starts in March and is characterized by progressively warmer, wetter and less windy
119 conditions until the monsoon is totally installed at the beginning of June. The pre-monsoon is then the
120 second wettest season after the monsoon with approximately one quarter of the annual precipitation on
121 the glacier (Khadka and others, 2022).

122 **3. DATA**

123 **3.1 Meteorological Data**

124 A network of automatic weather stations (AWSs) has been installed and gradually expanded since 2012 in
125 Mera Glacier catchment at different elevations and on various surfaces (Fig. 1). In this present study, we
126 mainly use data from two on-glacier AWSs, one located in the ablation area on Naulek branch at 5360 m
127 a.s.l., AWS-Low (hereafter referred as AWS-L; 4 years of data between November 2016 and October 2020),
128 and one located in the accumulation area at 5770 m a.s.l., AWS-High (hereafter referred as AWS-H; 3 years
129 of data between November 2017 and November 2020; Fig. S2). Both AWSs record air temperature (T),
130 relative humidity (RH), wind speed (u), incoming and outgoing longwave (LWin and LWout, respectively)
131 and shortwave (SWin and SWout, respectively) radiation (Table 1).

132 “Table 1 near here”

133 There are numerous data gaps in both records, due to AWS failure, power shortage during occasional
134 abundant snowfalls covering the solar panels for instance or sensor breakdowns (Table 1; Fig. 2 and see
135 <https://glacioclim.osug.fr/>). The largest data gap occurred at AWS-L, when the station fell down from 12
136 December 2017 to 24 November 2018. To fill these gaps, data from the off-glacier Mera La AWS was used.
137 Linear correlation relationships were established each month between the same variables from the two
138 stations from November 2016 to October 2020, at an hourly time step (Fig. S3 and Table S1). The
139 atmospheric pressure (Pa) measured at Mera La AWS is used at AWS-L without any interpolation, as both
140 AWSs are located less than 2 km apart at almost the same elevation (Table 1; Fig. 1).

141 The Khare Geonor station (4888 m a.s.l.) has been installed on 24-25 November 2016, 472 m lower in
142 elevation and ~3 km northwest of AWS-L. In Mera catchment, this is the only station of the network
143 recording all-weather precipitation, thanks to a weighing device. The precipitation data have been
144 corrected for undercatch following the method by Førland and others (1996) as a function of wind speed
145 and precipitation phase (liquid or solid) depending on air temperature (See the details in the supplement
146 of Khadka and others, 2022).

147 “Figure 2 near here”

148 **3.2 Spatial distribution of meteorological forcings**

149 Given the complexity and heterogeneity of the local climate and terrain, it is a challenging task to distribute
150 point data spatially. For air temperature, relative humidity and incoming longwave radiation, we derived
151 empirical linear relationships from the respective measurements of the two on-glacier AWSs installed with
152 a 410 m difference in altitude. To take advantage of the longest data series without gaps at AWS-H, we
153 calculate the gradients between 01 March 2018 and 28 February 2019, even though a major part of the
154 data from AWS-L is reconstructed over this period. Since AWS-L has a relatively longer and more consistent
155 dataset than AWS-H, we distribute meteorological data from this lower station across the glacier using
156 observed altitudinal gradients of air temperature, relative humidity, and incoming longwave radiation
157 (Table S2; Fig. S4). In meteorology, the dew-point temperature gradient is more commonly encountered
158 than the relative humidity gradient. However, in this particular study, the relative humidity gradient is
159 utilised because the COSIPY model is developed based on relative humidity input data. For completeness,
160 we also compute the dew-point temperature gradient from data collected at both stations, which we
161 subsequently convert into a relative humidity gradient. This converted gradient is comparable to the one

162 directly obtained from relative humidity measurements at AWS-L and AWS-H, that we use in our study
163 (Fig. S5 and corresponding supplementary text).

164 The incoming solar radiation has been distributed for each grid following the methods of Sauter and others
165 (2020), already tested and applied on Himalayan glaciers (e.g., Arndt and Schneider, 2023). First the
166 fraction of diffuse radiation (F_{diff}) is calculated based on Wohlfahrt and others (2016):

$$F_{diff} = e^{-e^{p1 - (p2 - p3CI)}} * (1 - p4) * p4 \quad (1)$$

167 Where $p1 = 0.1001$, $p2 = 4.7930$, $p3 = 9.4758$, $p4 = 0.2465$ are parameters from Wohlfahrt and others
168 (2016) and CI , for clearness index, is the ratio of incoming solar radiation to maximum incoming solar
169 radiation. F_{diff} may vary from 0 to 1. Second, the measured incoming shortwave radiation is split into
170 beam ($Rb = SWin * (1 - F_{diff})$) and diffuse ($Rd = SWin * F_{diff}$) radiation. Then, the corrected solar radiation
171 (Rc) is calculated on each grid based on Ham (2005).

$$Rc = Rb * cf + Rd \quad (2)$$

172 Where cf is the correction factor calculated based on the azimuth and the slope of each grid following
173 Ham (2005).

174 As our network does not allow to assess precipitation variations with elevation over Mera Glacier
175 catchment, precipitation amounts are assumed constant all over the catchment and equal to Khare
176 Geonor records. Similarly, wind speed is likely spatially variable due to terrain aspect, roughness and
177 heterogeneity but in first approximation, we had no choice but to consider the wind as constant over Mera
178 Glacier and equal to that at AWS-L. These first-order approximations are discussed in section 6.3.

179 **3.3 Mass balance data**

180 Mera Glacier has been monitored since 2007 at least once a year in November and its mass balance series
181 is one of the longest continuous field-based series of the Himalaya. Its glacier-wide mass balance is
182 obtained annually using the glaciological method based on a network of 16 ablation stakes and five
183 accumulation sites on average (Fig. 1). This glacier-wide mass balance series has been calibrated with the
184 2012-2018 geodetic mass balance (Wagnon and others, 2021). Over the period 2007-2023, the mean
185 corrected glacier-wide mass balance is equal to -0.42 ± 0.23 m w.e. a^{-1} , with only four positive mass balance
186 years out of 16. Our study period 2016-20 was characterized by constantly negative mass balance years

187 with a mean glacier-wide value of $-0.74 \pm 0.18 \text{ m w.e. a}^{-1}$, 2017-2018 being the most negative year (-0.92
188 $\pm 0.16 \text{ m w.e. a}^{-1}$) and 2019-2020 being the least negative ($-0.49 \pm 0.22 \text{ m w.e. a}^{-1}$) (Table 2). Between 2007
189 and 2023, the glacier has lost around 10 % of its surface area.

190 Point mass balances measured at each stake or at each accumulation site can exhibit significant spatial
191 variability depending on factors such as elevation, slope, aspect, and wind redistribution. Table 2 provides
192 the annual and mean values of point mass balances over the study period 2016-20 at the two on-glacier
193 AWSs. For AWS-L, it is computed by using all stake measurements available on Naulek branch between
194 5300 and 5380 m a.s.l., using a mean measured snow density of 370 kg m^{-3} and an ice density of 900 kg m^{-3} .
195 For AWS-H, point mass balances measured at sites located between 5750 and 5790 m a.s.l. in the vicinity
196 of the station are averaged, using depth averaged snow densities measured during each field campaign
197 (from 380 to 430 kg m^{-3}).

198 “Table 2 near here”

199 4. METHODS

200 4.1 Model Description (COSIPY)

201 In this study, we use COSIPY model, which is a python-based coupled snowpack and ice SEB model (Sauter
202 and others, 2020). The model is a one-dimensional multi-layer discretisation of the snowpack/ice column
203 that resolves the energy and mass conservation, and calculates the surface energy fluxes using input
204 meteorological variables as forcings. For spatially distributed simulations, the point model is run
205 independently at each point of the glacier domain, neglecting the lateral mass and energy fluxes. The
206 model's reliability has been validated across distinct contexts and geographical regions (Sauter and others,
207 2020; Blau and others, 2021; Arndt and others, 2021). COSIPY model calculates the energy available for
208 melt (QM) for each time step and is expressed as:

$$QM = SW_{net} + LW_{net} + QS + QL + QC + QR \quad (3)$$

209 where SW_{net} is the remaining net shortwave radiation at the surface after penetration inside the snow/ice
210 surface, LW_{net} is net longwave radiation and Q denotes the other heat fluxes of different subsequent
211 scripts S: sensible, L: latent, C: sub-surface (called ground-heat flux in Sauter and others, 2020), and R: rain
212 in W m^{-2} . All the fluxes are positive when directed towards the surface and negative away from the surface.

213 When the surface temperature is at the melting point and $QM > 0$, the excess energy is used to melt.
214 Additionally, COSIPY calculates a subsurface melt, that is calculated from the penetration of the incoming
215 shortwave radiation (Sauter and others, 2020). For the rest of the analysis, we refer to total melt as the
216 sum of surface and subsurface melt.

217 4.1.1 Model settings

218 The COSIPY model is used in its default configuration. The turbulent fluxes, QS and QL , are calculated as:

$$QS = \rho_{air} C_p C_s u (T - T_s) \quad (4)$$

$$QL = \rho_{air} L_v C_l u (q - q_s) \quad (5)$$

219 where ρ_{air} is air density (in kg m^{-3}); C_p is the specific heat of air at constant pressure (in $\text{J kg}^{-1} \text{K}^{-1}$) and L_v
220 is the latent heat of sublimation/vaporization (in J kg^{-1}). C_s and C_l are the dimensionless transport
221 coefficients calculated using the bulk method with initial roughness lengths taken from Mölg and others
222 (2012) and further calibrated (see section 4.2), q is the specific humidity of air (in g kg^{-1}), T_s and q_s are the
223 temperature (in $^{\circ}\text{C}$) and specific humidity at the surface, respectively. The bulk Richardson number has
224 been used to assess the stability correction.

225 The snowfall is distinguished from liquid precipitation using a logistic transfer function based on Hantel
226 and others (2000) (Fig. S6):

$$n = \frac{1}{2} \{ \tanh [((T - T_0) - T_{00}) s_0] + 1 \} \quad (6)$$

227 where n is the fraction of snowfall (1 when it is only snow, 0 if only rain and in between 0 and 1 if this is
228 mixed rain and snow), T_0 is the melting point (0°C), T_{00} is the center for snow transfer function (in $^{\circ}\text{C}$) and
229 s_0 is spread snow transfer function. The aging/decay of the snowpack's albedo is then based on Oerlemans
230 and Knap (1998), where it depends on the number of days after the last snowfall. Snow density is another
231 important property of snow, particularly for its liquid water content or thermal conductivity. It is obtained
232 by following Essery and others (2013). The default albedo and densification parameterizations used in this
233 study are described in the supplementary material (see additional text related to the method section p. 9-
234 10).

235 *4.1.2 Model description and initialisation*

236 We run COSIPY at point scale at AWS-L and in a distributed way over 51 glacierized grid points of
237 $0.003^{\circ} \times 0.003^{\circ}$ (0.0984 km^2) resolution (corresponding to a total glacier-covered area of 5.01 km^2),
238 resampled from Copernicus GLO-30 DEM (<https://doi.org/10.5270/ESA-c5d3d65>) using the glacier
239 outlines in 2012 (5.10 km^2) from Wagnon and others (2021). Additionally, the grid elevations were
240 adjusted downward by 19 meters to align with the elevation of AWS-L. The selection of this particular
241 resolution is a compromise between the computational time and a reasonable representation of the
242 topography. The model is run at an hourly time scale, independently for the four years of data, from 1
243 November of one year until 31 October of the following year over 2016-20, without spin-up time. We
244 impose a temperature of 265.16 K at the glacier sole because the glacier is cold-based (Wagnon and others,
245 2013). The model is initialised with 600 layers of glacier ice topped by a snowpack whose profile is specified
246 by the user. In our case, this profile is determined by the snow depth (Table 2), with each layer having an
247 optimal snow layer height of 0.1 m. The initial snow depth in the ablation zone is kept closest to the
248 observations made every November, corresponding to the snow depth measurement at AWS-L. Above
249 5750 m a.s.l., the model is initialised with a snow depth that increases by 20 cm per 100 m with altitude,
250 starting at 50 cm on 1 November at 5750 m a.s.l. (Table 2). This assumption is essential because it ensures
251 that there is always snow in the accumulation zone for the simulations. Even though annual observations
252 in November show that the snow line is always lower than 5750 m a.s.l., which is in line with this
253 assumption, the altitudinal gradient is not verifiable in the field. The snow depth in the accumulation zone
254 is probably greater than that used for the initialisation, as the firn-ice interface is several metres below the
255 glacier surface. However, for modelling purposes, the initial snow depth within this zone is of minimal
256 concern as accumulation consistently outweighs ablation, and the snow depth gradually synchronises with
257 the ongoing snowfall.

258 **4.2 Optimisation**

259 SEB models are sensitive to the choice of parameter sets (e.g., Zolles and others, 2019). Consequently,
260 model parameters need to be calibrated, and the model's ability to reproduce the glacier surface mass
261 balance needs to be evaluated. We optimise the model following a multi-objective optimisation procedure
262 using forcing data measured at AWS-L between 1 November 2018 and 31 October 2019, the mass balance
263 year with the least gaps and the most reliable dataset. The optimisation is performed based on the
264 maximum amount of data available i.e., observed albedo, surface temperature calculated from LWout

265 using the Stefan-Boltzmann equation with a surface emissivity of 0.99 (Blau and others, 2021), and point
266 mass balance at AWS-L (Table 2).

267 4.2.1 Parameters

268 There are many parameters in COSIPY and the eight important ones are listed in Table 3. To identify the
269 most sensitive ones among this set, we conducted 108 manual model runs at a point-scale, specifically at
270 AWS-L. In these runs, we alternatively and randomly explored various values for selected sensitive
271 parameters, focusing on five parameters related to albedo and three associated with roughness lengths.
272 This rigorous testing encompassed a plausible range of values, allowing us to qualitatively assess their
273 impact on the model's outcomes. These ranges of albedo parameters and roughness lengths are taken
274 from Mölg and others (2012). As we only have one level of wind speed measurement at AWS-L, roughness
275 lengths cannot be directly calculated at this site. Notably, the roughness lengths exhibited lower sensitivity
276 compared to the albedo parameters, which were identified as the most sensitive (in bold in Table 3). These
277 albedo parameters are known sensitive parameters for energy balance studies (e.g., Zolles and others,
278 2019). We then optimise these five parameters following the procedure described in section 4.2.2 starting
279 from a plausible range of values taken from the literature (Mölg and others, 2012; Zolles and others, 2019).
280 All other parameters are taken from the default settings, except those listed in bold in Table 3, that are
281 optimised.

282 “Table 3 near here”

283 4.2.2 Multi-objective optimisation

284 Multi-objective optimisation is a calibration method that enables the possibility of more than one optimal
285 solution and provides a way to evaluate a variety of parameter sets (Yapo and others, 1998; Rye and
286 others, 2012; Zolles and others, 2019). The multi-objective approach can be expressed as:

$$\text{minimise } \{f_1(\theta), f_2(\theta), \dots, f_n(\theta)\} \quad (7)$$

287 where $f_1(\theta), f_2(\theta), \dots, f_n(\theta)$ are n objective functions of model realisations of parameter sets θ . The
288 optimisation process combines multiple objectives into a single ideal through scalar aggregation. For this,
289 a weighted sum ($f_{\text{agg}}(\theta)$) is applied to find the minimum aggregate of different single objectives (Rye and
290 others, 2012):

$$\text{minimise } f_{agg}(\theta) = \{w_1 f_1(\theta), w_2 f_2(\theta), \dots, w_n f_n(\theta)\} \quad (8)$$

291 where w is the weight applied to all single objectives based on their performance and the arguments of
 292 the aggregating functions to obtain the Pareto solution (Pareto, 1971). With the multiple single objective,
 293 the selection of Pareto solution and multi-objective is more precise. Here, the multi-optimisation is done
 294 based on three objective metrics that compare the observation at AWS-L and model outputs:

$$f_1(\theta) = \left[\frac{\sum_{i=1}^n (x_i - \bar{x})(y_i - \bar{y})}{\sqrt{\sum_{i=1}^n (x_i - \bar{x})^2} \sqrt{\sum_{i=1}^n (y_i - \bar{y})^2}} \right]^2 \quad (9)$$

$$f_2(\theta) = \frac{1}{N} \left| \sum_{i=1}^N (y_i - x_i) \right| \quad (10)$$

$$f_3(\theta) = |(MB_{obs} - MB_{mod})| \quad (11)$$

295 where f_1 is the coefficient of determination (r^2) between the observed (x_i) and modelled (y_i) values of
 296 albedo and surface temperature (T_s), f_2 is the mean absolute error (MAE) between the observed (x_i) and
 297 modelled (y_i) values of both variables and f_3 is the absolute error (AE) between observed (MB_{obs}) and
 298 modelled (MB_{mod}) point mass balances.

299 “Figure 3 near here”

300 The simplest way to calibrate the model is to optimise the different objective functions for four study
 301 periods (4 years x 3 objective functions = 12 performances). This approach results in a large range of
 302 uncertainty with many sensitive parameters for different mass balance years. Similarly, the set of
 303 parameters optimised for one period may not perform better in another period, resulting in higher
 304 uncertainty (Soon and Madsen, 2005). However, by simulating Pareto solutions for individual mass balance
 305 years and evaluating the objective functions over the other years, it is possible to select the best set of
 306 parameters.

307 **4.3 Evaluation of the model at point and distributed scale**

308 First, we optimise the five sensitive model parameters highlighted in Table 3 at AWS-L for the 2018/19
 309 period. Second, we evaluate the model performance at point scale at AWS-L site for the other three mass
 310 balance years, systematically comparing measured and simulated albedo, surface temperature and point
 311 mass balance. Third, we run the model in a spatially distributed way and similarly evaluate it at point scale

312 at AWS-H site, over the three years of available data (2017-20). Finally, we also compare simulated mass
313 balance to measured surface mass balance at glacier-wide scale for each year between 2016 and 2020.
314 This allows us to test both the spatial and the temporal transferability of the model optimised parameters.

315 **4.4 Sensitivity analysis**

316 Our study aims to evaluate the sensitivity of the surface mass balance to changes in meteorological
317 forcings. In previous studies, the sensitivity to temperature or precipitation is usually assessed by a
318 constant change in temperature (e.g., $\pm 1-2$ °C) or a relative change in precipitation (e.g., $\pm 10-30$ %),
319 keeping all other meteorological variables unchanged at the same time (Kayastha and others, 1999; Mölg
320 and others, 2012; Sunako and others, 2019; Arndt and others, 2021; Srivastava and Azam, 2022; Gurung
321 and others, 2022; Arndt and Schneider, 2023). The main disadvantage of this method, hereafter referred
322 to as the classical method, is that perturbing a single meteorological variable breaks the physical links
323 between the meteorological variables, which is detrimental to the simulation of surface mass balance (e.g.,
324 Prinz and others, 2016; Clauzel and others, 2023). To overcome this issue, a number of methods were
325 developed to perturb meteorological data while preserving the link between variables (Sicart and others,
326 2010; Prinz and others, 2016; Autin and others, 2022). Here we both perturb the meteorological forcings
327 in a classical way and we produce synthetic scenarios, described below (see also Fig. S7 for a flow chart
328 explaining how scenarios are obtained).

329 *4.4.1 Classical scenarios*

330 For the classical sensitivity analysis method, the scenarios are developed by varying temperature by $\pm 1^\circ\text{C}$
331 and precipitation amount by ± 20 % for four mass balance years without changing the other meteorological
332 variables. In total, we produce 16 runs ($+ 1^\circ\text{C}$, $- 1^\circ\text{C}$, $+ 20$ % and $- 20$ % for each of the four years) between
333 2016 and 2020. In order to determine the sensitivity of the mass balance to temperature or precipitation,
334 it is then simply necessary to calculate the average anomaly in the mass balance over the four-year period
335 for each corresponding perturbation.

336 *4.4.2 Synthetic scenarios*

337 Utilising the initial four-year dataset, we performed a cyclic selection process, systematically considering
338 each month of the year commencing with November and concluding in October of the subsequent year.
339 During each cycle, we alternately chose data from the unaltered original dataset and data from the
340 warmest, coldest, wettest, or driest month within the four-year period (2016-20). This process allowed us

341 to generate synthetic annual datasets at an hourly resolution. By this way, we create 180 one-year-long
342 synthetic meteorological series, exploring a wide range of climatic variability from very warm to very cold
343 conditions, and from very dry to very wet conditions (see details below). For each scenario, for each
344 month, we keep original hourly data and we only shuffle the months from different years with each other.
345 In this way, both the physical integrity between meteorological variables and the weather conditions with
346 respect to the time of the year are preserved.

347 First, the four most extreme synthetic scenarios are developed by making one-year long series of hourly
348 forcing data that contain the most extreme months among the four years of data. For instance, the wet
349 scenario (hereafter referred as We_We) is obtained by combining the wettest (We) months: if November
350 2017 is the month with the maximum monthly amount of precipitation among the four months of
351 November of the 2016-20 series, all hourly forcing data from November 2017 are selected in scenario
352 We_We; then if December 2019 is the wettest of the four December months, then hourly data from
353 December 2019 will be selected as the second month of scenario We_We; etc. until October. In this way
354 the wet scenario We_We combining the hourly data of all meteorological variables from the 12 months
355 with the maximum monthly amount of precipitation is created. Similarly, we combine the hourly data of
356 all meteorological variables from the 12 driest months to create the dry scenario (D_D), or from the 12
357 warmest months to create the warm scenario (Wa_Wa), or from the 12 coldest months to create the cold
358 scenario (C_C).

359 Second, starting from these four extreme scenarios referred hereafter as baseline conditions, we also
360 create 48 additional scenarios by modifying some specific seasons. For instance, we keep the conditions
361 of the wet scenario We, except during one season, let's say the monsoon, where we decide to take the
362 conditions of the warm scenario Wa. The four considered seasons are winter (win), pre-monsoon (pre),
363 monsoon (mon), and melting season (melt). We decide not to consider the post-monsoon which is not
364 critical for the glacier mass balance because there is usually neither any large precipitation nor any large
365 melt but we prefer to introduce a six-month long melting season which we suspect to be more critical to
366 control the glacier mass balance. This melting season covers half of the year from May to October, the
367 only months where significant melt is observed in the field. The synthetic scenarios follow the naming
368 convention AB_x, where A is the climate baseline coming from the four extreme scenarios, so A is either
369 We, D, C, or Wa, B characterizes the conditions of the modified season i.e., B is also either We, D, C, or Wa
370 and X refers to the season that has been modified to create the additional scenario, so X is either win, pre,
371 mon, or melt. In case of the specific example described above, the scenario is named We_Wa_{mon} which

372 means that the dataset is one year long, using hourly forcing data from the wet scenario except during the
373 monsoon where the warmest months are selected. A can take 4 values, B can take 3 values and X can take
374 4 values (the number of values for B cannot be similar to that of A, otherwise we define one of the extreme
375 scenario), resulting in a total of $4 \times 3 \times 4 = 48$ scenarios.

376 Similarly, we also mix the original unshuffled data (U) from each year of the study period with extreme
377 months. U can be alternatively 2016/17, 2017/18, 2018/19 or 2019/20 respectively referred as 2017, 2018,
378 2019 or 2020. These scenarios follow the same naming convention, with U being an additional value for A
379 and B. For example, the scenario 2018_Wa_{mon} corresponds to the unchanged original data of the year
380 2017/18, except during the monsoon where data from the warmest months are selected. We obtain here
381 $4 \times 4 \times 4 = 64$ scenarios. Similarly, D_2020_{melt} corresponds to the driest months, where months of the melting
382 season have been replaced by the original 2019/20 data. Again, we obtain here $4 \times 4 \times 4 = 64$ scenarios. In
383 total, we have $4 + 48 + 64 + 64 = 180$ scenarios.

384 For each of these 180 synthetic annual datasets, we calculate the glacier-wide annual mass balance of
385 Mera Glacier using COSIPY and calculate the difference from the mean annual glacier-wide mass balance
386 simulated by COSIPY using the original 2016-20 dataset. We call this difference the mass balance anomaly.
387 Similarly, we have an anomaly for each forcing meteorological variable. We can now derive the mass
388 balance sensitivity to each meteorological variable by fitting a linear regression between the mass balance
389 anomaly and the anomaly of the variable under consideration. The slope of this linear relationship gives
390 the mass balance sensitivity to the given variable. The error bars on these sensitivities for ± 1 °C
391 temperature and ± 20 % precipitation variation have been calculated using the 99 % confidence interval,
392 given by three standard deviations, of this linear regression.

393 **5. RESULTS**

394 **5.1 Optimisation and evaluation**

395 *5.1.1 Optimisation*

396 The point-scale optimisation strategy at AWS-L results in a well identified group of parameter sets (Pareto
397 solutions) that minimise multiple objective functions simultaneously (Fig. 3). The objective functions of
398 each set of original parameters are largely scattered with the range of r^2 and MAE of albedo being 0.06-
399 0.54 and 0.11-0.25, respectively (Fig. 3a). Similarly for surface temperature, r^2 and MAE are in-between
400 0.81-0.92, and 1.37-3.24 °C, respectively (Fig. 3d). The range of AE is 0-3.92 m w.e. for the point mass

401 balance at AWS-L (Fig. 3b,c,e,f). The 200 solutions closest to the utopia point in terms of how well they
402 perform across all objective functions represent the Pareto solutions (Fig. 3: bold black dots). All these
403 multiple Pareto solutions are almost equally good and plausible. The metrics of the Pareto solutions are
404 less scattered than the original ensemble, with the range of r^2 and MAE of albedo being 0.31-0.54 and
405 0.11-0.15 (Fig. 3a), and the range of r^2 and MAE of surface temperature being 0.87-0.92 and 1.58-2.33 °C
406 (Table 4). The range AE is 0-1.28 m w.e. for the point mass balance at AWS-L (Table 4).

407 Since Pareto solutions perform well over all time and space ranges, the best parameter set among these
408 Pareto solutions is then chosen as the optimised set (Table 3). The r^2 and MAE between the observed
409 albedo and that resulting from the selected optimised parameter set are 0.48 and 0.12, respectively;
410 similarly, for surface temperature r^2 and MAE are 0.91 and 1.92 °C, respectively (Fig. 4), and AE for the
411 point mass balance is 0.17 m w.e. This final optimised set of parameters corresponds to a time scaling
412 factor of three days and a depth scaling factor of four centimetres for the albedo model (Oerlemans and
413 Knap, 1998) as well as values of albedo of snow (0.85), firn (0.55) and ice (0.30) similar to the default values
414 used in COSIPY (Table 3).

415 “Table 4 near here”

416 “Figure 4 near here”

417 *5.1.2 Glacier-wide simulation of COSIPY*

418 The good performance of COSIPY simulations at point scale with the optimal set of parameters does not
419 guarantee the good performance of the distributed simulations that rely on additional hypotheses, such
420 as the meteorological forcing distribution that changes the meteorological forcings even at AWS-L
421 location, because for instance SW_{in} is re-computed at AWS-L based on the slope and the aspect of the
422 considered grid cell. We thus evaluate the distributed COSIPY simulations over the period 2016-20 with
423 the albedo and surface temperature at AWS-L and AWS-H, and with the glacier-wide mass balance. r^2
424 (MAE) for albedo is 0.32 (0.15) and 0.16 (0.14) for the 2016/17 and 2019/20 years at AWS-L, respectively
425 (Fig. S8). At AWS-H, over the three-year period 2017-20, r^2 for albedo and surface temperature are 0.50
426 and 0.92 respectively, and the mean AE for 2016-20 at AWS-H is only 0.15 ± 0.14 m w.e.. The surface
427 temperature is always highly correlated with a low bias in both sites (Fig. S8). These metrics are close to
428 the ones from point-scale simulations.

429 “Figure 5 near here”

430 Additionally, we compare the observed and simulated surface point and glacier-wide mass balances. The
431 simulated point surface mass balances match well with the in-situ measurements obtained at stakes for
432 all the four years (Fig. 5 and 6). The location of the equilibrium line altitude is well represented in COSIPY
433 simulations and the general shape of the dependency of the surface point mass balance on elevation is
434 satisfyingly reproduced (Fig. 5). The glacier-wide mass balance from the model is the mean value from all
435 51 individual grid cells and it is compared to the in-situ glacier-wide mass balance taken from Wagnon and
436 others (2021). Over the four year period, the mean observed glacier-wide in-situ mass balance is $-0.74 \pm$
437 $0.18 \text{ m w.e. a}^{-1}$ (Table 2) and the simulated mass balance is $-0.66 \text{ m w.e. a}^{-1}$ with a standard deviation of
438 $\pm 0.26 \text{ m w.e. a}^{-1}$. The largest difference between the observed and modelled glacier-wide mass balance
439 happens in 2019/20, with the simulated mass balance being 0.22 m w.e. less negative than the observed
440 one (Fig. 5).

441 “Figure 6 near here”

442 **5.2 SEB and mass balance components**

443 *5.2.1 Seasonal and annual energy balance components*

444 Fig. 7 shows the monthly glacier-wide surface energy and mass balance components at Mera Glacier for
445 the period 2016-20, and Fig. S9-S16 are maps of the glacier, showing the distributed annual energy and
446 mass fluxes for each year of the study period. SW_{net} is the primary energy source available at the surface
447 throughout the year, the second energy source being the QS, that is significant only between November
448 and March. Along the year, SW_{in} is controlled by the position of the sun responsible for the potential SW_{in}
449 and also by cloudiness, explaining why it decreases from 274 W m^{-2} in the pre-monsoon to 195 W m^{-2}
450 during the monsoon (Table 5). Similarly, SW_{net} decreases from 83 W m^{-2} during the pre-monsoon to 61
451 W m^{-2} during the monsoon because of SW_{in} reduction rather than change in albedo (glacier-wide values
452 of 0.71 during the pre-monsoon and 0.70 during the monsoon). The change in air temperature and water
453 vapour (moisture) is responsible for a strong increase of LW_{in} from the pre-monsoon (217 W m^{-2}) to the
454 monsoon (296 W m^{-2}), the only season when LW_{in} nearly counterbalances the LW_{out} .

455 The total energy intake at the surface is highest and almost similar during the pre-monsoon (496 W m^{-2})
456 and the monsoon (491 W m^{-2}) (Table 5). However, the net all-wave radiation, calculated as the sum of
457 SW_{net} and LW_{net} , is 32 W m^{-2} during the pre-monsoon and 20 W m^{-2} higher during the monsoon. This
458 indicates that the change in cloud cover and atmospheric condition has a relatively minor effect on the

459 total energy absorbed at the glacier surface, but does impact the net all-wave radiation. In the pre-
460 monsoon, this net all-wave radiation is equally compensated by QL and QM ($\sim -16 \text{ W m}^{-2}$ each). During the
461 monsoon, LWnet and QL are both reduced or close to zero leaving all the energy available for melt with
462 an average energy value of -43 W m^{-2} . The contributions of QS and QC are always low during the pre-
463 monsoon and the monsoon, while the QR is negligible all the time.

464 The energy balance components vary across different glacier areas; they are analysed in the ablation area
465 at AWS-L and in the accumulation area at AWS-H. When considering the annual means, the magnitudes of
466 SWnet and QM are higher at AWS-L (93 and -34 W m^{-2} , respectively) than at AWS-H (61 and -15 W m^{-2} ,
467 respectively). LWnet, QL, and QS exhibit similar annual means throughout the year at both sites. At AWS-
468 L, SWnet remains similar during the pre-monsoon (87 W m^{-2}) and the monsoon (88 W m^{-2}) because the
469 decrease in SWin (287 W m^{-2} in the pre-monsoon and 201 W m^{-2} in the monsoon) is compensated by a
470 decrease in albedo (0.70 in the pre-monsoon and 0.56 in the monsoon). The albedo remains high at AWS-
471 H during the whole year, and there is thus a decrease of SWnet in the monsoon (43 W m^{-2}) compared to
472 the pre-monsoon (76 W m^{-2}). The variation of LWnet at AWS-L and AWS-H is rather small as the difference
473 between LWin and LWout remains similar. Comparing both sites, QL remains rather similar during all
474 seasons. QM dominates QL all year round except during the winter at AWS-L, but at AWS-H, QL always
475 dominates QM, except during the monsoon. QS is significant only during the cold months of the winter
476 and the post-monsoon, with a similar magnitude whichever the location. QC is positive and rather small
477 ($<5 \text{ W m}^{-2}$, slightly higher during the post-monsoon) all year round except during the monsoon at AWS-L
478 where it is slightly negative (Table 5).

479 “Table 5 near here”

480 “Figure 7 near here”

481 *5.2.2 Seasonal and annual mass balance components*

482 Table 6 lists the annual and seasonal mass balance components of Mera Glacier. After the direct
483 accumulation (through snowfalls) and surface melt on Mera Glacier, annual refreezing and sublimation
484 are two major mass balance components, refreezing being even higher than snowfalls. Indeed, at glacier
485 scale, 44% of the total (surface + sub-surface) melt refreezes annually. The glacier-wide sublimation is -
486 0.15 m w.e. and therefore contributes 23% of the total mass balance or 6% of the ablation terms (total
487 melt + sublimation).

488 Looking at seasonal scale, pre-monsoon and monsoon are important seasons in terms of mass balance
489 processes, as more than 86 % of solid precipitation falls and 84 % of annual melt happens from March to
490 September. However, post-monsoon is not completely negligible in terms of melt (-0.30 m w.e. or 14 % of
491 the annual melt). This melt is almost equal to the surface mass balance (-0.17 m w.e.) due to the limited
492 magnitude of the other processes, and in particular the limited refreezing in the snow free areas of the
493 glacier. The winter is characterized by limited mass balance processes, with approximately 11 % of the
494 annual solid precipitation and 2 % of the annual total melt (Table 6).

495 At glacier scale, the total melt (-0.42 m w.e.) and sublimation (-0.05 m w.e.) during the pre-monsoon are
496 balanced by the refreezing (0.30 m w.e.) and snowfall (0.14 m w.e.), leading to a near zero surface mass
497 balance (Table 6). The glacier-wide total melt during the monsoon is -1.42 m w.e., which is higher at AWS-
498 L (-2.15 m w.e.) and lower at AWS-H (-0.99 m w.e.). Depending on the presence and the state of a
499 snowpack (snow depth, density and temperature), melt water refreezes below the surface. Glacier-wide
500 refreezing is 0.49 m w.e. during the monsoon, it is lower at AWS-L (0.19 m w.e.) where ice is often exposed
501 at the surface, and higher at AWS-H (0.70 m w.e.) where there is always a snowpack with negative
502 temperature. The refreezing preserves 35 % (0.49 m w.e) of the total glacier-wide melt during the
503 monsoon; its relative contribution is higher at AWS-H (71 %) than at AWS-L (9 %).

504 The annual glacier-wide sublimation is -0.15 m w.e. and is nearly identical at both AWSs (-0.16 and -0.15
505 mm w.e. at AWS-L and AWS-H, respectively; Fig. S6). Most of the sublimation (93 % glacier-wide) happens
506 outside the monsoon, when cold, dry and windy conditions prevail. Wind is not spatially distributed in our
507 simulations, leading to rather homogeneous sublimation across the glacier. There are few exceptions, like
508 a slightly higher sublimation in winter at AWS-L (-0.07 m w.e.) than at AWS-H (-0.05 m w.e.) due to higher
509 roughness length linked to the surface state (exposed ice at AWS-L versus snow at AWS-H) and to the
510 mixing ratio that depends on the air temperature. Due to the lower wind speed, sublimation is insignificant
511 at both AWS sites during the monsoon (Table 6).

512 “Table 6 near here”

513 **5.3 Mass balance sensitivity to meteorological forcings**

514 *5.3.1 Link between meteorological forcing anomalies and mass balance anomalies*

515 In order to analyse the link between the different input meteorological variables and the outputs from the
516 simulations, we calculate anomalies of each variable from the 180 scenarios by subtracting the mean of

517 the original unshuffled 2016-20 simulations (Fig. 8). From all synthetic scenarios, the magnitude of
518 variation of air temperature is nearly ± 1 °C, whereas for precipitation, it varies from -35 to +55 % annually.
519 The anomalies of relative humidity (± 5 %) and incoming radiations (± 10 W m⁻²) are rather narrow. There
520 are many significant correlations ($p < 0.001$) between the anomalies of the different variables, suggesting
521 that they are likely to be physically related to each other. On an annual scale, the anomaly of air
522 temperature correlates significantly and positively with the wind speed and the air pressure anomalies,
523 and negatively with the precipitation and relative humidity anomalies. Regarding radiations that are
524 expected to have an impact on the mass balance, the SWin anomaly correlates significantly and negatively
525 with the relative humidity, the precipitation and the LWin anomalies. The LWin anomaly correlates
526 significantly and positively with the relative humidity and the precipitation anomalies, and negatively with
527 the SWin and wind speed anomalies.

528 The mass balance anomaly correlates significantly with the anomalies of every meteorological variables
529 except SWin (Fig. 8). The correlations between mass balance anomalies and those of LWin, atmospheric
530 pressure, or wind speed are moderate but significant, positive in case of LWin, and negative for the other
531 variables. The correlation between mass balance anomalies and air temperature is significant and highly
532 negative ($r = -0.79$). Mass balance anomalies are highly and positively correlated with those of precipitation
533 ($r = 0.87$) and relative humidity ($r = 0.84$; Fig. 8).

534 “Table 7 near here”

535 “Figure 8 near here”

536 *5.3.2 Mass balance sensitivity to air temperature and precipitation*

537 From the classical method, we find that perturbing the temperature by +1 (-1) °C leads to a change in
538 glacier-wide mass balance of -0.61 (+0.41) m w.e. (Table 7). A -20 (+20) % change in precipitation leads to
539 a -0.79 (+0.48) m w.e change in glacier-wide mass balance (Table 7). With the synthetic scenario method,
540 we find that a temperature change of +1 (-1) °C leads to a glacier-wide mass balance change of $-0.75 \pm$
541 0.17 ($+0.93 \pm 0.18$) m w.e., and a -20 (+20) % change in precipitation results in a mass balance change of $-$
542 0.60 ± 0.11 ($+0.52 \pm 0.10$) m w.e. Due to the physical link between variables, and in particular the negative
543 correlation between temperature and precipitation, we find that the sensitivity of mass balance to
544 temperature is significantly higher when calculated from synthetic scenarios than from the classical

545 method, especially in case of cooling. For precipitation, it is significantly reduced in case of a precipitation
546 deficit but almost unchanged in case of an increase.

547 This synthetic scenario approach allows to derive mass balance sensitivities to any meteorological variable,
548 as long as a significant correlation exists between the anomalies of mass balance and the variable under
549 consideration. In particular, as we find a high correlation between mass balance and relative humidity
550 anomalies, we can assess also the mass balance sensitivity to this variable: a -4 (+4) % change in RH
551 corresponds to a -1.02 (+1.38) m w.e. change in mass balance. However, we caution on the interpretation
552 of these correlations, as most of the input meteorological variables covary, the correlations may be
553 significant, but they do not show a causal relationship, that needs to be discussed in the light of the
554 knowledge of the processes (see discussion section).

555 “Figure 9 near here”

556 *5.3.3 Specific meteorological conditions leading to the most positive/negative mass balances*

557 From the synthetic scenarios, the annual glacier-wide mass balances range from -1.76 to 0.54 m w.e. (Fig.
558 9 and Fig. S17), which is a wider range than the historically measured glaciological mass balance since 2007
559 (min = -0.92 m w.e. in 2017/18 and max = 0.26 m w.e. in 2010/11; Wagnon and others, 2021). The
560 simulated annual mass balances are compared with the original mean annual glacier-wide mass balance
561 of -0.66 m w.e. (Table 6) over the 2016-20 study period, referred hereafter as the reference year. Most of
562 scenarios that have warm or dry conditions as a baseline correspond to the first category of scenarios
563 characterised with negative mass balances ranging from -1.76 to -0.81 m w.e. They have a positive SWnet
564 anomaly compared to the reference year (+2 to +17 W m⁻²), associated either with a change in air
565 temperature toward a warming (-0.71 to +1.13 °C) or to a decrease in snowfall (0 to -0.29 m w.e.) or to
566 both, resulting in a low glacier-wide albedo (0.53 to 0.64). With more energy intake, melting is enhanced,
567 and due to the reduced snowfalls, ice is more exposed at the glacier surface favoring runoff, and in turn
568 less than 46 % of this meltwater refreezes, ultimately leading to the most negative glacier-wide mass
569 balances (Fig. S17).

570 The second category of scenarios corresponds to glacier-wide mass balances from -0.80 to -0.25 m w.e.
571 close to that of the reference year. Here, we find scenarios combining a baseline and a seasonal
572 component that would normally lead to opposite mass balance responses such as dry with wet conditions
573 or warm with cold conditions (e.g., Wa_We_{mon}, D_We_{mon}, Wa_We_{win}, D_C_{win}). We also find the majority of

574 scenarios that have the unperturbed data as baseline (Fig. 9 and Fig. S17). The mass balance is affected
575 equally but in an opposite direction by the temperature anomalies (-0.97 and +1.02 °C) and the
576 precipitation anomalies (-0.16 to +0.23 m w.e.). In this category, the refreezing ranges from 37 to 56 % of
577 total melt, which is close to that of the reference year (44 %), and the ranges of SWnet (-8 to +6 W m⁻²)
578 and LWnet (-4 to +3 W m⁻²) anomalies are small (Fig. 8).

579 The third category corresponds to positive or near-balanced glacier-wide mass balances (> -0.25 m w.e.)
580 mostly produced by scenarios with wet or cold baselines. They have temperature anomalies between -
581 1.00 and +0.52°C and precipitation anomalies between -0.04 and +0.45 m w.e. (Fig. 9 and Fig. S17). The
582 higher amount of snowfall increases the accumulation, increases the albedo, and in turn decreases the
583 SWnet (-19 to -4 W m⁻²). In addition, the refreezing is high (46-71 % of total melt). Overall, the scenarios
584 with a wet year baseline always create a mass balance that is close to balance, and specifically, the highest
585 positive mass balance is produced by the wettest conditions all year round (scenario WeWe) (Fig. 9 and
586 Fig. S17).

587 For all scenarios, we find that the mass balance is primarily influenced by the baseline conditions, and not
588 by the seasonal variation. We do not find any season that has an influence larger than the other ones (Fig.
589 S17). In particular, when we look at the scenarios of unperturbed data with seasonal variations, we find
590 that winter seems to have as much influence, if not even more influence, than the other seasons on the
591 mass balance (Fig. S17). This result is rather counter intuitive, as most of the mass balance processes
592 happen in monsoon and pre-monsoon (e.g., Fig. 8).

593 Regarding the classical scenarios, as expected, both -20 % and +1 °C scenarios produce negative mass
594 balances, but less extreme than the dry and warm synthetic scenarios. In contrast, both +20 % and -1 °C
595 classical scenarios are characterised by near-balanced mass balances, far from the positive glacier-wide
596 mass balances obtained with the wet and cold scenarios. The energy and mass fluxes in the classical
597 scenarios are also comparable to those of the synthetic scenarios. The LWnet is similar in all classical
598 scenarios. However, SWnet is 13 W m⁻² higher and refreezing is 25 % lower in the -20 % precipitation and
599 +1 °C scenarios than those in the +20 % and -1 °C scenarios.

600 **6. DISCUSSION**

601 **6.1 Surface energy and mass balance components of Mera Glacier, and comparison with other similar** 602 **studies in HKH**

603 It is difficult to compare different glacier surface energy and mass balance analyses rigorously across the
604 same region because study periods are never similar. Moreover, temporal (multi-annual, annual, or
605 seasonal) and spatial (point scale or glacier-wide) resolutions are often different and not comparable
606 (Table 8). In HKH region, the seasonality of precipitation has a strong impact on the energy and mass
607 balance components. In the western Himalaya, the winter precipitation dominates the annual
608 accumulation, and sublimation strongly contributes to the ablation processes (Mandal and others, 2022;
609 Srivastava and Azam, 2022; Oulkar and others, 2022). In the Central Himalaya, the glaciers are summer
610 accumulation type with significant longitudinal variability in mean summer temperature, which has the
611 strongest impact on mass balance sensitivity (Sakai and Fujita, 2017). Still, precipitation, which depends
612 on the monsoon intensity and duration, is a key variable governing the energy and mass balance of glaciers
613 through the albedo effect and its control on the refreezing (Shaw and others, 2022).

614 The pattern of surface energy and mass balance over the whole Mera Glacier confirms what has already
615 been observed on other glaciers of HKH (Table 8, which is an update of Table 4 of Azam and others, 2014,
616 with the location of glaciers given in Fig. S18). Overall, the radiative fluxes strongly dominate the SEB, and
617 control the amount of energy available for melt (Fig. 7). Between the pre-monsoon and the monsoon, with
618 the gradual establishment of the dense cloud cover typical of this latter wet and warm season, incoming
619 shortwave radiation gradually loses intensity, replaced at the same time by increasing incoming longwave
620 radiation, resulting in a constantly high amount of radiative energy available for the glacier. This amount
621 of energy decreases with elevation mainly because albedo is higher in the accumulation zone, where ice
622 is never exposed at the surface. Turbulent fluxes are only significant out of the monsoon, contributing to
623 bring additional energy toward the surface by sensible heat flux (Fig. 7). Contrary to glaciers in the western
624 Himalaya where resublimation occasionally occurs during the monsoon (Azam and others, 2014), on Mera
625 Glacier, the latent heat flux is always negative which means that sublimation is a non-negligible process of
626 mass loss, especially during seasons with strong wind (winter and post-monsoon), like on Zhadang and
627 Parlung No 4 glaciers on the southeast Tibetan Plateau (Mölg and others, 2012; Sun and others, 2014; Zhu
628 and others, 2018). On Mera Glacier, glacier-wide sublimation accounts for 23 % of the glacier-wide mass
629 balance (Table 6), in agreement with previously published values in the Himalaya (e.g., Gurung and others,
630 2022; Srivastava and Azam, 2022) or lower than that of Shruti Dhaka Glacier in the western Himalaya (55
631 %; Oulkar and others 2022). However, this value on Mera Glacier is under-estimated because wind speed
632 strongly increases with elevation (Khadka and others, 2022), an effect that has not been taken into account
633 in our study. Refreezing is also an important process, because at annual and glacier-wide scales, as much
634 as 44 % of meltwater refreezes on Mera Glacier, with a clear increase of this percentage with elevation

635 (Table 6). This finding is again in agreement with other studies in the region (Stigter and others, 2018;
636 Kirkham and others, 2019; Bonekamp and others, 2019; Veldhuijsen and others, 2022; Arndt and
637 Schneider, 2023). It is noteworthy mentioning that sublimation and refreezing are two important
638 processes for glaciers in this region but they are not included in empirical degree-day models (Litt and
639 others, 2019). Moreover, refreezing is always parameterised in a more or less sophisticated way in physical
640 snowpack models, but field experiments are crucially missing to evaluate the accuracy of such
641 parameterisations.

642 “Table 8 near here”

643 **6.2 Mass balance sensitivity to different meteorological variables and comparison with other studies in** 644 **HKH**

645 *6.2.1 Mass balance sensitivity of Mera Glacier to meteorological variables*

646 Estimating the sensitivity of glacier mass balance to a change in temperature and/or precipitation is a
647 classical problem in glaciology (e.g., Ohmura and others, 1992). Different approaches have been
648 implemented in HKH to assess the glacier mass balance sensitivity at different scales (e.g., Sakai and Fujita,
649 2017; Wang and others, 2019; Arndt and others, 2021; Gurung and others, 2022). However, the classical
650 approach (perturbing temperature and precipitation by certain values or percentages), which involves
651 perturbing individual meteorological variables while keeping others unchanged, has been criticised due to
652 the interconnectedness of these variables (Nicholson and others, 2013; Prinz and others, 2016). For
653 example, changing air temperature directly impacts the water vapor ratio of the atmosphere, which can
654 ultimately affect the turbulent heat fluxes.

655 For Mera Glacier, we find strong correlations among the meteorological variables, which makes difficult
656 to decipher their individual effects on mass balance. Notably, the negative correlation between
657 temperature and precipitation anomalies ($r = -0.56$; slope of the linear relationship: $-0.16 \text{ m w.e. } ^\circ\text{C}^{-1}$) leads
658 to larger mass balance sensitivities to temperature when this relationship is preserved (Table 7). The mass
659 balance sensitivity to SWin is unexpectedly limited ($-0.06 \text{ m w.e. a}^{-1} (\text{W m}^{-2})^{-1}$; $r = -0.22$) due to the role of
660 albedo. Indeed, the correlation between albedo anomalies and mass balance anomalies is very high ($r =$
661 0.97) showing that the surface state, that depends primarily from the amount of snowfalls, is more
662 important than the actual incoming shortwave radiative flux. Despite its direct contribution to the SEB,
663 LWIn correlates positively with mass balance due to its strong correlation with precipitation. One limitation

664 of our approach is that we can virtually find sensitivities of the mass balance to any input variable, as long
665 as a correlation exists. For instance, the strong sensitivity to the relative humidity shown in Fig. 8 should
666 not be interpreted as an expected change in mass balance due to a change in relative humidity. Instead it
667 shows that the relative humidity is closely tied to the other meteorological variables, and that
668 meteorological conditions that favor high relative humidity also favor positive mass balances.

669 Another interesting feature is the asymmetry towards negative values in the sensitivities to temperature
670 with the classical method (Table 7). While continental and sub-continental glaciers typically exhibit less
671 sensitivity to negative temperature changes (e.g., Arndt and Schneider, 2023; Wang and others, 2019),
672 maritime glaciers tend to have symmetrical sensitivity, especially when estimated with degree-day models
673 (Wang and others, 2019). However, with the synthetic scenario approach, we find the opposite asymmetry
674 for temperature sensitivity (Table 7), likely due to the correlations between precipitation and temperature.
675 This leads to higher negative mass balances than the simple +1 °C perturbation (Fig. 8), indicative of the
676 maritime climate setting for Mera Glacier. Regarding precipitation, its sensitivity is asymmetric towards
677 negative values with both methods (Table 7). It is clearly due to albedo feedback effects in the model,
678 which are poorly represented in degree-day models that predict a symmetric sensitivity to precipitation
679 (e.g., Wang and others, 2019).

680 *6.2.2 Mass balance sensitivity comparison with other studies in HKH*

681 The impact of temperature and precipitation changes on mass balance depends on the climate of the
682 region, but it can be attenuated or exacerbated depending on the glacier's morphology and topography
683 (Brun and others, 2019). Contrary to glaciers located in arid cold climates less sensitive to temperature
684 changes (Ohmura and others, 1992), those affected by the Indian summer monsoon, such as Mera Glacier,
685 are sensitive to both temperature and precipitation (Fujita, 2008; Johnson and Rupper, 2020; Arndt and
686 others, 2021). With higher temperature, first less precipitation falls as snow and in turn accumulation is
687 reduced, and second and more important, more shortwave radiation is absorbed through lower albedo
688 leading to enhanced melt (Fujita, 2008). Still the mass balance sensitivity to temperature and precipitation
689 varies among different glaciers. The glacier-wide sensitivity of Mera Glacier to changes in temperature and
690 precipitation is of the same order of magnitude as other glaciers in HKH, even though it is noteworthy to
691 mention that these glacier sensitivities have been assessed through the classical method and in turn are
692 not directly comparable (Fig. 10, Table S3).

693 For instance, on Mera Glacier, with the synthetic scenarios approach, a ± 1 °C temperature perturbation
694 has greater impact than that of a ± 20 % precipitation change, which is mostly the case for glaciers on Fig.
695 10, especially those located in Nepal. However, this pattern differs for glaciers in the Indian western
696 Himalaya, which mostly exhibit lower sensitivities, sometimes higher for precipitation than for
697 temperature like Shruti Dhaka Glacier (Oulkar and others, 2022). Surprisingly, Arndt and Schneider (2023)
698 find extreme sensitivities of glacier-wide mass balances to warming or to increase in precipitation for
699 glaciers in the Central Himalaya (Yala and Halji glaciers) or Nyainqentanglha Range (Zhadang Glacier)
700 compared to what we observe on Mera Glacier, although all these glaciers are submitted to rather humid
701 monsoon dominated conditions.

702 Our approach with the synthetic scenarios does not allow to investigate whether the sensitivity changes
703 linearly. It is well established that the sensitivity to temperature is nonlinear and much higher for larger
704 temperature changes (e.g., Arndt and Schneider, 2023). As we rely only on existing observations, we
705 cannot assess what would be the other meteorological variables in a +2 or +3 °C climate setting. Directions
706 to overcome this issue could be to investigate the links between glaciers' response to synoptic variables
707 (e.g., Mölg and others, 2012; Zhu and others, 2022), to investigate specific monsoon characteristics and
708 their impacts on the mass balance (e.g., Shaw and others, 2022), or to force glacier mass balance models
709 with downscaled global circulation model outputs that preserve the physical relationships between
710 variables (e.g., Bonekamp and others, 2019; Clauzel and others, 2023). Furthermore, the size of the glacier
711 plays a role on its mass balance sensitivity. Glaciers with a higher accumulation area, such as Shruti Dhaka,
712 Trambau, and Mera glaciers, exhibit a lower sensitivity than glaciers whose accumulation zone is strongly
713 reduced, such as Zhadang and Halji glaciers (Zhu and others, 2018; Sunako and others, 2019; Arndt and
714 others, 2021; Srivastava and Azam, 2022).

715 “Figure 10 near here”

716 **6.3 Limitations of our approach**

717 Simulating the distributed surface energy and mass balance of a glacier presents numerous challenges and
718 limitations. One striking example is the relatively large difference between the simulated and observed
719 glacier-wide mass balances for the year 2019/20, where COSIPY simulated mass balance is 0.22 m w.e.
720 larger than the observed one. While we do not have a definitive explanation for such a discrepancy, we
721 can list a number of sources of errors in our approach. Uncertainties arise primarily from (i) the model's

722 process representation, (ii) in-situ data, (iii) their spatial distribution over the glacier area, and (iv) the
723 model's initial conditions.

724 One crucial process in snowpack modelling is the decay of snow albedo over time. COSIPY implements the
725 Oerlemans parameterisation (Oerlemans and Knap, 1998), which has known limitations in certain climate
726 contexts (e.g. Voordendag and others, 2021; Wang and others, 2022). Typically, albedo parameters are
727 fixed or adopted from previous studies using COSIPY or any other energy balance model. However, here,
728 we optimised these parameters at AWS-L before distributing the meteorological forcings. The snow aging
729 and depth scaling factors used in this study fall within the range of commonly used factors (Sauter and
730 others, 2020; Arndt and others, 2021; Wang and others, 2022; Sherpa and others, 2023), but differ slightly
731 from those used in other studies (Sauter and others, 2020; Arndt and others, 2021; Potocki and others,
732 2022). Although the model can accurately predict albedo at a point scale, it is sometimes misrepresented
733 (Fig. S8). The lack of robust parameterisation and uncertainties surrounding the amount of snow deposited
734 on the glacier surface and its redistribution by the wind contribute to this issue.

735 Additionally, refreezing is another poorly constrained process. In HKH region, refreezing has primarily been
736 assessed using models (Steiner and others, 2018; Kirkham and others, 2019; Saloranta and others, 2019;
737 Veldhuijsen and others, 2022), rather than snowpack temperature and density measurements, as is done
738 in the seasonal snowpack (e.g. Pfeffer and Humphrey, 1996). Specific experiments should be conducted
739 to evaluate the effects of refreezing on glaciers, particularly to determine whether meltwater percolates
740 below the previous year's horizon and contributes to internal accumulation. Additionally, COSIPY lacks
741 certain processes, such as wind erosion and wind-driven snow densification. These processes can be very
742 important, particularly during the post-monsoon and winter seasons due to the strong winds at high
743 elevations (Litt and others, 2019; Brun and others, 2023; Sherpa and others, 2023). During November field
744 campaigns, wind erosion features such as sastrugis are frequently observed in the accumulation area of
745 Mera Glacier.

746 Distributing meteorological data over a rough terrain is one of the most challenging task. The spatial
747 distribution of the meteorological data based on a single vertical gradient throughout the year is somehow
748 questionable (section 3.2). Additionally, applying a vertical gradient to distribute meteorological variables
749 weakens the physical links between them, as already discussed in the sensitivity analysis. For the study
750 period and the range of elevation of Mera Glacier, the vertical gradients for temperature, relative
751 humidity, and LWin exhibit high variability (Fig. S3). To derive the gradients, we selected the year with the

752 minimum gaps at AWS-H despite a large portion of the data at AWS-L being reconstructed at that time.
753 Additionally, the T/RH sensor was not artificially ventilated at AWS-H, which introduces some
754 measurement uncertainty. Therefore, we tested a range of gradients to distribute T [-6.5 to -4.2 °C km⁻¹]
755 and RH [-25 to 0 % km⁻¹]. In alpine environments, LWin provides large amounts of melt energy, especially
756 in the ablation area (through valley side walls) and can dominate the energy balance of snow or glacier
757 surfaces. LWin is highly sensitive to surface melt when the atmosphere is saturated, particularly during the
758 monsoon (Sicart and others, 2010). On Mera Glacier, the daily LWin gradient as a function of elevation
759 varies greatly from day to day and season to season, with a minimum of -41 W m⁻² km⁻¹ observed during
760 the monsoon. Various LWin gradients have been tested within the [-40 to 0 W m⁻² km⁻¹] range and
761 optimised to -25 W m⁻² km⁻¹ (Table S2). In conclusion, there is no ideal method for spatially distributing
762 meteorological variables on a complex glacier surface that extends over a large altitudinal range. On Mera
763 Glacier, two on-glacier AWSs enable us to provide reasonable vertical gradients of temperature, relative
764 humidity, and longwave incoming radiation. These gradients are highly variable in time and likely in space
765 as well. To maintain simplicity in our modelling approach, we prefer to use a single gradient for these
766 variables instead of using temporally or spatially variable gradients. The use of variable gradients would
767 require a denser observation network than the two AWSs we currently have. Additionally, using different
768 gradients would alter the set of optimised parameters without necessarily affecting the final results.

769 The depletion of precipitation as a function of elevation in the upper Khumbu region is still a matter of
770 debate due to the lack of reliable data at high elevations, difficulties in correcting the undercatch of snow,
771 and comparing precipitation records obtained with different devices (Salerno and others, 2015; Perry and
772 others, 2020). On the Mera catchment, there is only one all-weather rain gauge located at 4888 m a.s.l.,
773 just below the glacier. The precipitation recorded at this station is considered constant across the glacier
774 surface. The distribution of precipitation is clearly more complex due to the rough topography (Immerzeel
775 and others, 2014) and snow redistribution by wind. We prefer not to apply any vertical precipitation
776 gradient, as it would complicate the modelling and increase equifinality issues, as with other
777 meteorological variables. Similarly, applying a vertical gradient of wind speed based on records at AWS-L
778 and AWS-H is not recommended due to the site-specific nature of the records (Shea et al., 2015).
779 Therefore, like precipitation, wind speed is assumed to be constant and equal to the wind velocity at AWS-
780 L across the glacier. Given that wind speed mainly affects turbulent fluxes, which are of secondary
781 importance compared to radiative fluxes, any assumptions made only impact the total sublimation and its
782 spatial distribution.

783 To initialise the model, the snow depth on each grid cell at the start of the simulation, specifically on 1
784 November, must be known. As field trips typically occur around mid-November each year, and November
785 is a relatively dry month with minimal melting, snow depth initialisation is based on direct observations
786 performed around 15 days later than the initialisation date. However, this method is not entirely error-
787 free as not all grid cells are surveyed and precipitation or wind drift may have occurred between 1
788 November and the survey date. Such error may have large impacts over the entire simulation period when
789 a surface is initially recognized snow free although it is not, or vice versa.

790 In COSIPY, between 10 and 20 % of SWnet penetrates below the surface and is partly reflected at different
791 depths within the snowpack or the ice (van den Broeke and Bintanja, 1995). This amount of shortwave
792 radiation is not accounted for in the outtake term Q_{out} of Table 5, which explains why Q_{in} and Q_{out} do
793 not exactly compensate each other. Therefore, the energy balance is not perfectly closed in the COSIPY
794 model (e.g., Arndt and others, 2021).

795 **7. CONCLUSION**

796 The COSIPY energy and mass balance model was applied to Mera Glacier in the Central Himalaya, Nepal.
797 In-situ meteorological datasets were used, recorded both on and off the glacier at different elevations
798 ranging from 4888 m a.s.l. (for precipitation) to 5770 m a.s.l. The data was collected from 1 November
799 2016 to 31 October 2020 at an hourly time step. The model parameters were optimised at the point scale
800 using data from AWS-L at 5360 m a.s.l. over the year 2018/19. A multi-objective optimisation was
801 employed, and the albedo aging and snow depth factors were selected as the most sensitive parameters
802 and then calibrated. The model was validated both at the point scale with multiple AWS measurements
803 (albedo and surface temperature recorded at 5360 and 5770 m a.s.l.) and at the glacier scale with annual
804 point mass balance measurements obtained at various elevations. The validation indicates that the model
805 effectively simulates the annual glacier-wide mass balance of Mera Glacier, with a simulated mean value
806 of $-0.66 \text{ m w.e. a}^{-1}$ for 2016-20 compared to the observed value of $-0.74 \text{ m w.e. a}^{-1}$.

807 The SEB over Mera Glacier is dominated by radiative fluxes, which are responsible for almost all the energy
808 available during the monsoon, the main melting season. From the pre-monsoon to the monsoon, with the
809 increasing cloudiness, incoming shortwave radiation gradually decreases in intensity in favor of incoming
810 longwave radiation thus maintaining a large amount of energy available for melt. Turbulent fluxes are only
811 significant outside the monsoon. The sensible heat is an energy source at the surface whereas the latent
812 heat flux is always negative. Sublimation is therefore an important ablation process, especially during the

813 windy months of the post-monsoon and winter. Annually and at glacier scale, refreezing is a crucial
814 process, because on average 44 % of meltwater refreezes, with a large positive gradient with altitude.

815 To investigate the sensitivity of glacier mass balance to changes in temperature and precipitation, we
816 generated 180 different scenarios by shuffling our four-year dataset. We aggregated warm, cold, dry, or
817 wet months alternatively, depending on the seasons. These scenarios allowed us to explore a wide range
818 of conditions, from very dry and warm to very cold and wet. As a result, the glacier-wide mass balances of
819 Mera Glacier ranged from -1.76 to $+0.54$ m w.e. a^{-1} . The mass balance sensitivity to meteorological
820 variables can be quantified from these synthetic scenarios. A temperature change of $+1$ °C (-1 °C) results in
821 a change of -0.75 ± 0.17 ($+0.93 \pm 0.18$) m w.e. in glacier-wide mass balance, while a precipitation change
822 of $+20$ % (-20 %) results in a change of $+0.52 \pm 0.10$ (-0.60 ± 0.11) m w.e. in mass balance. Compared to
823 the classical approach, the sensitivity of the mass balance is more pronounced with temperature, but not
824 significantly different with precipitation. Similar to other glaciers with summer accumulation, Mera Glacier
825 is highly sensitive to both temperature and precipitation.

826 To evaluate the mass balance sensitivity to any meteorological variables, it is advantageous to generate
827 scenarios based on real in-situ data. This not only helps to quantify these sensitivities more accurately but
828 also to explore the inter-relationships between variables. Our study demonstrates, for instance, that
829 temperature has a negative correlation with precipitation. Therefore, classical sensitivity approaches that
830 alter temperature and precipitation independently are likely to be biased. It is worth noting that long-term
831 high-quality datasets are necessary to apply such synthetic method approach. We are lucky enough to
832 have a long-term dataset on Mera Glacier, but we encourage to maintain and develop similar
833 observational networks on other glaciers in HKH, in order to compare glaciers and to assess whether
834 sensitivities obtain locally on a glacier can be extrapolated regionally. Currently, we cannot be certain that
835 this sensitivity is not specific to Mera Glacier.

836 Like any modelling, our approach has limitations inherent to the model used, the quality of input data,
837 their spatial distribution, and the choice of initial conditions. These limitations are difficult to quantify, but
838 our method allows us to provide an accuracy range for the results based on a 99 % confidence interval. A
839 potential next step in this study would be to conduct an uncertainty analysis to assess the weight of all
840 potential errors related to the model and data, as well as to evaluate the equifinality of the results.
841 However, this is beyond the scope of the present study. Nonetheless, such an analysis would be valuable,
842 as many modelling approaches encounter similar issues.

843 **Acknowledgements**

844 This work has been supported by the French Service d'Observation GLACIOCLIM (part of IR OZCAR), the
845 French National Research Agency (ANR; iFROG project, grant no. ANR-21-CE01-0012), and a grant from
846 Labex OSUG@2020 (Investissements d'avenir ANR10-LABX56). This work would not have been possible
847 without the International Joint Lab Water-Himal (principal investigators D. Shrestha, and P. Wagnon)
848 supported by IRD and all the efforts from people in the field: porters, students, and helpers who are greatly
849 acknowledged here. A. Khadka is grateful to IRD and Perpetual Planet program supported by the National
850 Geographic Society and Rolex for providing financial support for his PhD. He benefited from the support
851 of the International Centre for Integrated Mountain Development (ICIMOD), which is funded in part by the
852 governments of Afghanistan, Bangladesh, Bhutan, China, India, Myanmar, Nepal, and Pakistan. We thank
853 the Nepal Mountaineering Association, which provides free permits to conduct field work on Mera peak.
854 We want to thank Anselm Arndt for the support in understanding and modifying the initial condition on
855 the COSIPY. Also, we would like to thank Simon Gascoin, Jakob Steiner, Argha Banejee, Arindan Mandal
856 and one anonymous referee who's comments greatly helped to improve the work.

857 **Author contribution**

858 PW initiated and DS supported the monitoring program on Mera Glacier. PW, FB and AK jointly designed
859 the study. AK performed the analysis, under the supervision of FB and PW, with the support of TS. AK
860 prepared all the figures and wrote the first draft of the manuscript. AK, FB and PW jointly developed the
861 discussion and interpretation of the results. All authors participated in some field campaigns, and
862 contributed to the analysis and to the paper writing.

863 **Data availability**

864 The data utilised in this study are accessible through the GLACIOCLIM database
865 (<https://glacioclim.osug.fr/Donnees-himalaya>). The model outputs are available at
866 <https://doi.org/10.5281/zenodo.10053093>.

867 **References**

868 **Acharya A and Kayastha RB** (2019) Mass and Energy Balance Estimation of Yala Glacier (2011-2017),
869 Langtang Valley, Nepal. *mdpi: Water* **11**(6). doi:10.3390/w11010006.

- 870 **Ageta Y and Higuchi K** (1984) Estimation of mass balance components of a summer-accumulation type
871 glacier in the Nepal Himalaya. *Geografiska Annaler, Series A* **66 A(3)**, 249–255.
872 doi:10.1080/04353676.1984.11880113.
- 873 **Arndt A, Scherer D and Schneider C** (2021) Atmosphere driven mass-balance sensitivity of Halji glacier,
874 Himalayas. *Atmosphere* **12(4)**. doi:10.3390/ATMOS12040426.
- 875 **Arndt A and Schneider C** (2023) Spatial pattern of glacier mass balance sensitivity to atmospheric forcing
876 in High Mountain Asia. *Journal of Glaciology*, 1–18. doi:10.1017/JOG.2023.46.
- 877 **Autin P, Sicart JE, Rabatel A, Soruco A and Hock R** (2022) Climate Controls on the Interseasonal and
878 Interannual Variability of the Surface Mass and Energy Balances of a Tropical Glacier (Zongo Glacier,
879 Bolivia, 16°S): New Insights From the Multi-Year Application of a Distributed Energy Balance Model.
880 *Journal of Geophysical Research: Atmospheres* **127(7)**, 1–21. doi:10.1029/2021JD035410.
- 881 **Azam MF and others** (2014) Processes governing the mass balance of Chhota Shigri Glacier (western
882 Himalaya, India) assessed by point-scale surface energy balance measurements. *The Cryosphere* **8**,
883 2195–2217. doi:10.5194/tc-8-2195-2014.
- 884 **Azam MF, Wagnon P, Vincent C, Ramanathan A, Linda A and Singh VB** (2014) Reconstruction of the
885 annual mass balance of Chhota Shigri glacier, Western Himalaya, India, since 1969. *Annals of*
886 *Glaciology* **55(66)**, 69–80. doi:10.3189/2014AoG66A104.
- 887 **Blau MT, Turton J V., Sauter T and Mölg T** (2021) Surface mass balance and energy balance of the 79N
888 Glacier (Nioghalvfjærdsfjorden, NE Greenland) modeled by linking COSIPY and Polar WRF. *Journal of*
889 *Glaciology*, 1–15. doi:10.1017/jog.2021.56.
- 890 **Bonekamp PNJ, de Kok RJ, Collier E and Immerzeel WW** (2019) Contrasting Meteorological Drivers of
891 the Glacier Mass Balance Between the Karakoram and Central Himalaya. *Frontiers in Earth Science*
892 **7**, 107. doi:10.3389/feart.2019.00107.
- 893 **van den Broeke MR and Bintanja R** (1995) The surface energy balance of antarctic snow and blue ice.
894 *Journal of Applied Meteorology* **34**, 902–926.
- 895 **Brun F and others** (2019) Heterogeneous Influence of Glacier Morphology on the Mass Balance
896 Variability in High Mountain Asia. *Journal of Geophysical Research: Earth Surface* **124(6)**, 1331–

- 897 1345. doi:10.1029/2018JF004838.
- 898 **Clauzel L and others** (2023) Sensitivity of Glaciers in the European Alps to Anthropogenic Atmospheric
899 Forcings: Case Study of the Argentière Glacier. *Geophysical Research Letters* **50**(13),
900 e2022GL100363. doi:10.1029/2022GL100363.
- 901 **Essery R, Morin S, Lejeune Y and B Ménard C** (2013) A comparison of 1701 snow models using
902 observations from an alpine site. *Advances in Water Resources* **55**, 131–148.
903 doi:10.1016/j.advwatres.2012.07.013.
- 904 **Favier V, Wagnon P, Chazarin JP, Maisincho L and Coudrain A** (2004) One-year measurements of surface
905 heat budget on the ablation zone of Antizana Glacier 15, Ecuadorian Andes. *Journal of Geophysical*
906 *Research Atmospheres* **109**(18). doi:10.1029/2003JD004359.
- 907 **Førland EJ and others** (1996) Manual for operational correction of Nordic precipitation data. *DNMI-*
908 *Reports* (24(96), 66). doi:Report Nr. 24/96, DNMI, P.O. Box 43, Blindern, Oslo, Norway,.
- 909 **Fugger S, Fyffe CL, Fatichi S, Miles E, Mccarthy M and Shaw TE** (2022) Understanding monsoon controls
910 on the energy and mass balance of glaciers in the Central and Eastern Himalaya. *The Cryosphere* **16**,
911 1631–1652. doi:https://doi.org/10.5194/tc-16-1631-2022.
- 912 **Fujita K** (2008) Effect of precipitation seasonality on climatic sensitivity of glacier mass balance. *Earth*
913 *and Planetary Science Letters* **276**(1–2), 14–19. doi:10.1016/j.epsl.2008.08.028.
- 914 **Gurung TR, Kayastha RB, Fujita K, Joshi SP, Sinisalo A and Kirkham JD** (2022) A long-term mass-balance
915 reconstruction (1974–2021) and a decadal in situ mass-balance record (2011–2021) of Rikha Samba
916 Glacier, central Himalaya. *Journal of Glaciology*, 1–14. doi:10.1017/JOG.2022.93.
- 917 **Ham J** (2005) Useful equations and tables in micrometeorology. *Wiley Online Library*.
918 <https://access.onlinelibrary.wiley.com/doi/abs/10.2134/agronmonogr47.c23>.
- 919 **Hamm A and others** (2020) Intercomparison of gridded precipitation datasets over a sub-region of the
920 Central Himalaya and the Southwestern Tibetan Plateau. *Water* 2020, Vol. 12, Page 3271 **12**(11),
921 3271. doi:10.3390/w12113271.
- 922 **Hantel M, Ehrendorfer M and Haslinger A** (2000) Climate sensitivity of snow cover duration in Austria.

923 *International Journal of Climatology* **20**(6), 615–640. doi:10.1002/(SICI)1097-
924 0088(200005)20:6<615::AID-JOC489>3.0.CO;2-0.

925 **Huintjes E, Neckel N, Hochschild V and Schneider C** (2015) Surface energy and mass balance at
926 Purogangri ice cap, central Tibetan Plateau, 2001–2011. *Journal of Glaciology* **61**(230), 1048–1060.
927 doi:10.3189/2015JOG15J056.

928 **Huintjes E and others** (2015) Evaluation of a Coupled Snow and Energy Balance Model for Zhadang
929 Glacier, Tibetan Plateau, Using Glaciological Measurements and Time-Lapse Photography. *Arctic,*
930 *Antarctic, and Alpine Research* **47**(3), 573–590. doi:10.1657/AAAR0014-073.

931 **Johnson E and Rupper S** (2020) An Examination of Physical Processes That Trigger the Albedo-Feedback
932 on Glacier Surfaces and Implications for Regional Glacier Mass Balance Across High Mountain Asia.
933 *Frontiers in Earth Science* **8**. doi:10.3389/FEART.2020.00129/FULL.

934 **Kayastha RB, Ohata T and Ageta Y** (1999) Application of a mass-balance model to a Himalayan glacier.
935 *Journal of Glaciology* **45**(151), 559–567. doi:10.3189/s002214300000143x.

936 **Khadka A, Wagnon P, Brun F, Shrestha D, Lejeune Y and Arnaud Y** (2022) Evaluation of ERA5-Land and
937 HARv2 reanalysis data at high elevation in the upper Dudh Koshi basin (Everest region, Nepal).
938 *Journal of Applied Meteorology and Climatology* **61**(8), 931–954. doi:10.1175/jamc-d-21-0091.1.

939 **Kirkham JD and others** (2019) Near real-time measurement of snow water equivalent in the Nepal
940 Himalayas. *Frontiers in Earth Science* **7**(July), 1–18. doi:10.3389/feart.2019.00177.

941 **Lejeune Y, L'hote Y, Etchevers P, Wagnon P, Chazarin J-P and Chevallier P** (2007) Constitution d'une
942 base de données météorologiques sur un site andin de haute altitude : le site du Charquini, 4795 m,
943 Bolivie. **318**.

944 **Li S, Yao T, Yang W, Yu W and Zhu M** (2018) Glacier energy and mass balance in the inland Tibetan
945 Plateau: Seasonal and interannual variability in relation to atmospheric changes. *Wiley Online*
946 *Library* **123**(12), 6390–6409. doi:10.1029/2017JD028120.

947 **Litt M, Shea J, Wagnon P, Steiner J, Koch I and Stigter EE** (2019) Glacier ablation and temperature
948 indexed melt models in the Nepalese Himalaya. *nature Scientific Report*.
949 <https://www.nature.com/articles/s41598-019-41657-5>.

- 950 **Lutz A, Immerzeel W, Shrestha A and Bierkens M** (2014) Consistent increase in High Asia's runoff due to
951 increasing glacier melt and precipitation. *Nature Climate Change* 2014 **4**, 587–592.
- 952 **Mandal A and others** (2022) 11-year record of wintertime snow surface energy balance and sublimation
953 at 4863 m a.s.l. on Chhota Shigri Glacier moraine (western Himalaya, India). *The Cryosphere*.
954 doi:10.5194/tc-2021-386.
- 955 **Marzeion B, Jarosch AH and Hofer M** (2012) Past and future sea-level change from the surface mass
956 balance of glaciers. *Cryosphere* **6**(6), 1295–1322. doi:10.5194/TC-6-1295-2012.
- 957 **Mölg T, Maussion F, Yang W and Scherer D** (2012) The footprint of Asian monsoon dynamics in the mass
958 and energy balance of a Tibetan glacier. *The Cryosphere* **6**, 1445–1461. doi:10.5194/tc-6-1445-
959 2012.
- 960 **Nicholson LI, Prinz R, Mölg T and Kaser G** (2013) Micrometeorological conditions and surface mass and
961 energy fluxes on Lewis Glacier, Mt Kenya, in relation to other tropical glaciers. *The Cryosphere* **7**(4),
962 1205–1225. doi:10.5194/TC-7-1205-2013.
- 963 **Oerlemans J and others** (1999) Glacio-meteorological investigations on Vatnajökull, Iceland, Summer
964 1996: An overview. *Boundary-Layer Meteorology* **92**(1), 3–24. doi:10.1023/A:1001856114941.
- 965 **Oerlemans J and Knap W** (1998) A 1 year record of global radiation and albedo in the ablation zone of
966 Morteratschgletscher, Switzerland. *Journal of Glaciology* **44**(147), 231–238.
967 doi:10.1017/S0022143000002574.
- 968 **Oerlemans J and Reichert BK** (2000) Relating glacier mass balance to meteorological data by using a
969 seasonal sensitivity characteristic. *Journal of Glaciology* **46**(152), 1–6.
970 doi:10.3189/172756500781833269.
- 971 **Ohmura A, Kasser P and Funk M** (1992) Climate at the Equilibrium Line of Glaciers. *Journal of Glaciology*
972 **38**(130), 397–411. doi:10.3189/S0022143000002276.
- 973 **Oulkar SN and others** (2022) Energy fluxes, mass balance, and climate sensitivity of the Sutri Dhaka
974 Glacier in the western Himalaya. *Frontiers in Earth Science* **0**, 1298.
975 doi:10.3389/FEART.2022.949735.

- 976 **Pareto V** (1971) Manual of political economy, Macmillan, London.
- 977 **Pepin N and others** (2015) Elevation-dependent warming in mountain regions of the world. *Nature*
978 *Climate Change* 2015 5:5 **5**(5), 424–430. doi:10.1038/nclimate2563.
- 979 **Perry LB and others** (2020) Precipitation Characteristics and Moisture Source Regions on Mt. Everest in
980 the Khumbu, Nepal. *One Earth* **3**(5), 594–607. doi:10.1016/j.oneear.2020.10.011.
- 981 **Prinz R, Nicholson LI, Mölg T, Gurgiser W and Kaser G** (2016) Climatic controls and climate proxy
982 potential of Lewis Glacier, Mt. Kenya. *The Cryosphere* **10**, 133–148. doi:10.5194/tc-10-133-2016.
- 983 **Rounce DR, Hock R and Shean DE** (2020) Glacier Mass Change in High Mountain Asia Through 2100
984 Using the Open-Source Python Glacier Evolution Model (PyGEM). *Frontiers in Earth Science* **7**.
985 doi:10.3389/FEART.2019.00331.
- 986 **Rye CJ, Willis IC, Arnold NS and Kohler J** (2012) On the need for automated multiobjective optimization
987 and uncertainty estimation of glacier mass balance models. *Journal of Geophysical Research: Earth*
988 *Surface* **117**(F2), 2005. doi:10.1029/2011JF002184.
- 989 **Sakai A and Fujita K** (2017) Contrasting glacier responses to recent climate change in high-mountain
990 Asia. *Scientific Reports* **7**(1), 1–8. doi:10.1038/s41598-017-14256-5.
- 991 **Sauter T, Arndt A and Schneider C** (2020) COSIPY v1.3 – an open-source coupled snowpack and ice
992 surface energy and mass balance model. *Geoscientific Model Development* **13**(11), 5645–5662.
993 doi:10.5194/gmd-13-5645-2020.
- 994 **Shaw TE and others** (2022) Multi-decadal monsoon characteristics and glacier response in High
995 Mountain Asia. *Environmental Research Letters* **17**(10), 104001. doi:10.1088/1748-9326/AC9008.
- 996 **Shea JM, Wagnon P, Immerzeel WW, Biron R, Brun F and Pellicciotti F** (2015) A comparative high-
997 altitude meteorological analysis from three catchments in the Nepalese Himalaya. *International*
998 *Journal of Water Resources Development* **31**(2), 174–200. doi:10.1080/07900627.2015.1020417.
- 999 **Shea JM, Immerzeel WW, Wagnon P, Vincent C and Bajracharya S** (2015) Modelling glacier change in
1000 the Everest region, Nepal Himalaya. *The Cryosphere* **9**, 1105–1128. doi:10.5194/tc-9-1105-2015.
- 1001 **Sicart JE, Hock R, Ribstein P and Chazarin JP** (2010) Sky longwave radiation on tropical Andean glaciers:

- 1002 Parameterization and sensitivity to atmospheric variables. *Journal of Glaciology* **56**(199), 854–860.
1003 doi:10.3189/002214310794457182.
- 1004 **Srivastava S and Azam MF** (2022) Mass- and Energy-Balance Modeling and Sublimation Losses on
1005 Dokriani Bamak and Chhota Shigri Glaciers in Himalaya Since 1979. *Frontiers in Water* **4**(April), 1–
1006 21. doi:10.3389/frwa.2022.874240.
- 1007 **Stigter EE and others** (2018) The Importance of Snow Sublimation on a Himalayan Glacier. *Frontiers in*
1008 *Earth Science* **6**. doi:10.3389/feart.2018.00108.
- 1009 **Sun W and others** (2014) Ablation modeling and surface energy budget in the ablation zone of Laohugou
1010 glacier No. 12, western Qilian mountains, China. *Annals of Glaciology* **55**(66), 111–120.
1011 doi:10.3189/2014AoG66A902.
- 1012 **Sunako S, Fujita K, Sakai A and Kayastha RB** (2019) Mass balance of Trambau Glacier, Rolwaling region,
1013 Nepal Himalaya: In-situ observations, long-term reconstruction and mass-balance sensitivity.
1014 *Journal of Glaciology* **65**(252), 605–616. doi:10.1017/jog.2019.37.
- 1015 **Thakuri S and others** (2014) Tracing glacier changes since the 1960s on the south slope of Mt. Everest
1016 (central Southern Himalaya) using optical satellite imagery. *The Cryosphere* **8**(4), 1297–1315.
1017 doi:10.5194/tc-8-1297-2014.
- 1018 **Veldhuijsen SBM, De Kok RJ, Stigter EE, Steiner JF, Saloranta TM and Immerzeel WW** (2022) Spatial and
1019 temporal patterns of snowmelt refreezing in a Himalayan catchment. *Journal of Glaciology* **68**(268),
1020 369–389. doi:10.1017/jog.2021.101.
- 1021 **Wagnon P and others** (2021) Reanalysing the 2007-19 glaciological mass-balance series of Mera Glacier,
1022 Nepal, Central Himalaya, using geodetic mass balance. *Journal of Glaciology* **67**(261), 117–125.
1023 doi:10.1017/jog.2020.88.
- 1024 **Wagnon P and others** (2013) Seasonal and annual mass balances of Mera and Pokalde glaciers (Nepal
1025 Himalaya) since 2007. *Cryosphere* **7**(6), 1769–1786. doi:10.5194/tc-7-1769-2013.
- 1026 **Wang R, Liu S, Shangguan D, Radić V and Zhang Y** (2019) Spatial Heterogeneity in Glacier Mass-Balance
1027 Sensitivity across High Mountain Asia. *Water* **11**(4), 776. doi:10.3390/W11040776.

- 1028 **Wohlfahrt G, Albin H, Georg N, Katharina S, Enrico T and Peng Z** (2016) On the energy balance closure
 1029 and net radiation in complex terrain. *Agricultural and Forest Meteorology* **226**, 37–49.
 1030 doi:10.1016/j.agrformet.2016.05.012.
- 1031 **Yapo PO, Gupta HV and Sorooshian S** (1998) Multi-objective global optimization for hydrologic models.
 1032 *Journal of Hydrology* **204**(1–4), 83–97. doi:10.1016/S0022-1694(97)00107-8.
- 1033 **Zhu M and others** (2022) Possible Causes of Anomalous Glacier Mass Balance in the Western Kunlun
 1034 Mountains. *Journal of Geophysical Research: Atmospheres* **127**(7), e2021JD035705.
 1035 doi:10.1029/2021JD035705.
- 1036 **Zhu M, Yang W, Yao T, Tian L, Thompson LG and Zhao H** (2021) The Influence of Key Climate Variables
 1037 on Mass Balance of Naimona'nyi Glacier on a North-Facing Slope in the Western Himalayas. *Journal*
 1038 *of Geophysical Research: Atmospheres* **126**(7). doi:10.1029/2020JD033956.
- 1039 **Zhu M, Yao T, Xie Y, Xu B, Yang W and Yang S** (2020) Mass balance of Muji Glacier, northeastern Pamir,
 1040 and its controlling climate factors. *Journal of Hydrology* **590**(June), 125447.
 1041 doi:10.1016/j.jhydrol.2020.125447.
- 1042 **Zhu M, Yao T, Yang W, Xu B, Wu G and Wang X** (2018) Differences in mass balance behavior for three
 1043 glaciers from different climatic regions on the Tibetan Plateau. *Climate Dynamics* **50**(9–10), 3457–
 1044 3484. doi:10.1007/s00382-017-3817-4.
- 1045 **Zhu M, Yao T, Yang W, Maussion F, Huintjes E and Li S** (2015) Energy- and mass-balance comparison
 1046 between Zhadang and Parlung No. 4 glaciers on the Tibetan Plateau. *Journal of Glaciology* **61**(227),
 1047 595–607. doi:10.3189/2015JOG14J206.
- 1048 **Zolles T, Maussion F, Peter Galos S, Gurgiser W and Nicholson L** (2019) Robust uncertainty assessment
 1049 of the spatio-temporal transferability of glacier mass and energy balance models. *The Cryosphere*
 1050 **13**(2), 469–489. doi:10.5194/TC-13-469-2019.

1051
 1052 **List of figure captions**

1053 **Fig. 1.** Map of Mera Glacier showing the network of ablation stakes (blue dots) and accumulation pits (cyan
 1054 diamonds). The stake location and number are taken from November 2020. The number of stakes vary
 1055 from year to year, due to total excavation, reinstallation at the original location, snow burial or destruction.

1056 The pink stars represent the locations of different AWSs with their respective photos and dates (a. Khare
1057 Geonor, b. Mera La AWS, c. AWS-H, and d. AWS-L). The outline of Mera Glacier is from 2018 with a total
1058 area of 4.84 km², and the background image was acquired by Sentinel-2 on 24 November 2018. Elevation
1059 lines are extracted from the 2012 Pléiades DEM (Wagnon and others, 2021). The inset map gives the
1060 location of Mera Glacier in Nepal (black square) and the glacierised areas from RGI6 (shaded blue areas).

1061 **Fig. 2.** Hourly data from 1 November 2016 to 31 October 2020 of (a) air temperature (T), (b) relative
1062 humidity (RH), (c) wind speed (u), (d) incoming shortwave radiation (SWin), (e) incoming longwave
1063 radiation (LWin) at AWS-L, (f) atmospheric pressure (P_a) at Mera La AWS and (g) precipitation (P) at Khare
1064 Geonor. Orange shaded areas indicate data gaps at AWS-L, which have been filled by Mera La AWS data
1065 using linear interpolation, and the light blue shaded areas in panel (g) visualise the monsoons.

1066 **Fig. 3.** Solution space for the multi-objective optimisation for the period 1 November 2018 – 31 October
1067 2019. One dot represents results obtained with one set of parameters, and bold black and red dots define
1068 the Pareto solution space and optimised solution, respectively. Plots show the scatter plot between a) 1-
1069 r² and MAE from albedo comparison, b) MAE from albedo comparison and AE from mass balance
1070 comparison, c) AE of mass balance comparison vs 1-r² from albedo, d) 1-r² and MAE from surface
1071 temperature comparison, e) MAE from surface temperature comparison and AE from mass balance and f)
1072 AE of mass balance vs 1-r² from surface temperature comparison.

1073 **Fig. 4.** Mean daily snow albedo (top) and surface temperature (bottom) from observation (Obs., black line)
1074 and simulated with COSIPY between 1 November 2018 and 31 October 2019 at AWS-L. r² and MAE
1075 represent the correlation coefficient and mean absolute error between the observed and simulated
1076 variables, respectively. The red thick line and the brown thin lines represent the simulated variables using
1077 the final optimised parameter set and using all other solution spaces, respectively.

1078 **Fig. 5.** In-situ (blue dots) and simulated at each grid cell (red dots) point mass balances as a function of
1079 elevation on Mera Glacier for each year of the 2016-20 period. MB is the glacier-wide mass balance
1080 obtained from field measurements (blue text) (Wagnon and others, 2021) and simulated with COSIPY (red
1081 text). Also shown are the hypsometries of Mera Glacier used for in-situ glacier-wide mass balance
1082 calculations (light blue histograms) and for COSIPY (light brown histograms).

1083 **Fig. 6.** Distributed simulated annual mass balance (MB, in m w.e.) for each year of the study period. Also
1084 shown as white circles are the point mass balance observations (ablation stakes and accumulation pits)

1085 with the inside colour corresponding to the respective annual measurement. The glacier outlines (black)
1086 is from Wagnon and others (2021).

1087 **Fig. 7.** Glacier-wide monthly (a) energy fluxes, (b) mass fluxes and (c) mass balance from November 2016
1088 to October 2020 on Mera Glacier (left panels) and mean monthly annual cycle (right panels). SWnet = net
1089 shortwave radiation, LWnet = net longwave radiation, QL = latent heat flux, QS = sensible heat flux, QC =
1090 subsurface heat flux, QR = rain heat flux, QM = available melt energy at the surface, SnowF. = solid
1091 precipitation, Subl. = sublimation, Surf. M. = melt at surface, Sub S. M. = subsurface melt and Refr. =
1092 refreezing. Blue shaded areas visualise the monsoons.

1093 **Fig. 8.** Scatter plot between anomalies of different input variables and glacier-wide mass balance
1094 anomalies for the 180 synthetic runs. Also shown are the Pearson correlation coefficients between the
1095 series of annual anomalies. The black lines represent the linear regressions and the grey shaded areas
1096 indicate the standard error. The anomalies of each variable are calculated by subtracting the mean of the
1097 original unshuffled 2016-20 simulation. (stars represent significance levels, accordingly: * = 0.05, ** = 0.01,
1098 *** = 0.001).

1099 **Fig. 9.** Glacier-wide (a) energy fluxes, (b) mass flux components, and (c) mass balance (MB) from (left
1100 panels) 12 selected synthetic scenarios (in red, grey, and blue, on the x-axis), as well as (right panels) from
1101 the four mean classical scenarios (in black) and the reference year (RY, in green, on the x-axis). The results
1102 from the classical scenarios or the reference year have been averaged over the four years 2016-20. Based
1103 on the MB results, 12 synthetic scenarios are selected (four corresponding to the most negative MBs, four
1104 from the middle of the MB set with moderately negative MBs, and four most positive MBs) out of the 180
1105 scenarios (all visible in Fig S17). The colour code of synthetic scenarios visualises the MB range, from the
1106 most negative (red), to the most positive (blue), grey being intermediate and moderately negative. 2019
1107 and 2020 represent the 2018/19 and 2019/20 mass balance years, respectively. SWnet = net shortwave
1108 radiation, LWnet = net longwave radiation, QL = latent heat flux, QS = sensible heat flux, QC = subsurface
1109 heat flux, QR = rain heat flux, QM = available melt energy at the surface, SnowF. = solid precipitation, Subl.
1110 = sublimation, Surf. M. = melt at surface Sub S. M. = subsurface melt and Refr. = refreezing.

1111 **Fig. 10.** Location of glaciers where studies of mass balance sensitivities have been conducted in the
1112 Himalaya and Tibetan Plateau regions. Each panel gives the mass balance sensitivity to temperature and
1113 precipitation of each glacier, with the associated reference. Table S3 lists all these glaciers, and provides
1114 additional information.

1115 **List of tables**

1116 **Table 1.** List of the different AWSs operating on Mera Glacier, or in its vicinity, with their elevations, operating periods, list of
 1117 sensors and associated meteorological variables used as forcing, optimisation or validation data of the SEB model. T = air
 1118 temperature, RH = relative humidity, u = wind speed, SWin = incoming shortwave radiation, SWout = outgoing shortwave radiation,
 1119 LWin = incoming longwave radiation, LWout = outgoing longwave radiation, P_a = atmospheric pressure and P = precipitation). The
 1120 numbers in brackets indicate the data gap of the variables (second column) or the uncertainty of each sensor provided by the
 1121 manufacturer (third column).

Station	Variables (gap % during the study period)	Sensors (uncertainty)
Khare Geonor 4888 m a.s.l. 25 Nov 2016 – 18 Nov 2020 Off-glacier, on a grassy surface	P (0)	GEONOR T-200BM (±15%)
Mera La AWS 5350 m a.s.l. 01 Nov 2016 – 31 Oct 2020 Off-glacier, on a rocky surface	T (0), RH (0) u (1) SWin (0) LWin (0) P _a (0)	Vaisala-HMP45C* (±0.2°C; ±2%) Young 05103-5 (±0.3 m/s) Kipp&Zonen CNR4 (±3%) CS100 (±2.0 hPa)
AWS-L 5360 m a.s.l. 01 Nov 2016 – 31 Oct 2020 On-glacier (ablation area)	T (23.2), RH (23.2) u (25.8) SWin (23.8), SWout (24.0) LWin (24.0), LWout (24.0)	Vaisala-HMP45C* (±0.2°C; ±2%) Young 05103-5 (±0.3 m/s) Kipp&Zonen CNR4 (±3%)
AWS-H 5770 m a.s.l. 11 Nov 2017 – 18 Nov 2020 On-glacier (accumulation area)	T (17.1), RH (17.1) u (17.1) SWin (17.2), SWout (17.2) LWin (17.1), LWout (27.8)	Vaisala-HMP45C (±0.2°C; ±2%) Young 05103-5 (±0.3 m/s) Kipp&Zonen CNR4 (±3%)

1122 * artificially aspired during daytime

1123 **Table 2.** Glacier-wide mass balance for Mera Glacier, point mass balance at AWS-L (obtained by averaging all stake measurements
 1124 on Naulek branch between 5300 and 5380 m a.s.l.) and at AWS-H (obtained by averaging stake measurements close to AWS-H,
 1125 from 5750 to 5790 m a.s. l.), as well as snow depths in the ablation area (annually measured during field campaigns in November)
 1126 and in the accumulation area (assumed for the model). An ice density of 900 kg m⁻³ and measured snow densities were used to
 1127 compute point mass balances (370 kg m⁻³ for Naulek, and 380 to 430 kg m⁻³ for the accumulation area). The error range for point
 1128 mass balances is the standard deviation of all measurements.

Glaciological mass balance of Mera Glacier						
	2016/17	2017/18	2018/19	2019/20	2016-20	
Glacier-wide mass balance* (m w.e. a ⁻¹)	-0.76 ± 0.16	-0.92 ± 0.16	-0.80 ± 0.19	-0.49 ± 0.22	-0.74 ± 0.18	

Mean point mass balance around AWS-L (m w.e. a ⁻¹)	-2.26 ± 0.12	-2.34 ± 0.19	-2.27 ± 0.10	-2.10 ± 0.24	-2.24 ± 0.09
Mean point mass balance around AWS-H (m w.e. a ⁻¹)	0.16 ± 0.01	-0.08 ± 0.07	0.12 ± 0.13	0.35 ± 0.12	0.14 ± 0.15
Snow depth in the ablation zone (< 5750 m a.s.l.) used for the model initialisation (m)	0.50	0.12	0	0.20	
Snow depth in the accumulation zone (> 5750 m a.s.l.) used for the model initialisation (m)	0.50 m at 5750 m a.s.l. and an additional 0.20 m for each 100 m increase in altitude				

1129 * updated from Wagnon and others (2021)

1130 **Table 3.** List of selected parameters used in COSIPY, and manually tested before running our optimisation procedure. In bold are
1131 the 5 most sensitive parameters that are optimised from a plausible range of values (Min-Max range, taken from the Mölg and
1132 others (2012) and used in this present study). The investigated range of max-min values for the roughness lengths is also shown.

Parameters	Min	Max	Optimised/default
Fresh snow albedo	0.82	0.88	0.85
Firn Albedo	0.50	0.60	0.55
Ice albedo	0.25	0.35	0.30
Albedo time scaling factor (days)	3	9	3
Albedo depth scaling factor (cm)	2	14	4
Roughness length for fresh snow (mm)	0.19	0.29	0.24
Roughness length for firn (mm)	1.5	6.5	4
Roughness length for ice (mm)	0.7	2.7	1.7

1133 **Table 4.** The range of different objective function values in the first 200 Pareto solution space for 2018/19 period at AWS-L.

Objective function	Albedo	Surface temperature	Mass balance
$f_1(\theta)$	0.31-0.54	0.87-0.92	
$f_2(\theta)$	0.11-0.15	1.58-2.33 °C	
$f_3(\theta)$			0-1.28 m w.e.

1134 **Table 5.** Annual and seasonal surface energy fluxes ($W m^{-2}$) and their contribution to the total energy intake (Q_{in}) and outtake
1135 (Q_{out}) over the whole Mera Glacier area, at AWS-L and at AWS-H. The annual values are calculated between 1 November to 31

1136 October of the following year, using all data over the study period. The negative (-) sign indicates the energy loss from the surface.

1137 Winter = Dec-Feb, Pre-monsoon = Mar-May, Monsoon = Jun-Sep, Post-monsoon = Oct-Nov.

	SWin	SWout	SWnet	albedo	LWin	LWout	LWnet	QL	QS	QC	QR	QM	Qin	Qout
Annual values (W m⁻²)														
Glacier-wide mean	215	-139	76	0.65	229	-273	-43	-13	4	4	0	-22	453	-447
AWS-L	227	-134	93	0.59	235	-278	-43	-14	4	3	0	-34	470	-460
AWS-H	218	-157	61	0.72	225	-269	-44	-13	4	5	0	-15	453	-454
Seasonal Glacier-wide (W m⁻²)														
Winter	183	-107	76	0.59	172	-237	-66	-22	13	4	0	-2	372	-368
Pre-monsoon	274	-191	83	0.71	217	-268	-51	-16	1	4	0	-17	496	-491
Monsoon	195	-133	61	0.70	296	-306	-10	-2	0	2	0	-43	491	-485
Post-monsoon	217	-121	96	0.56	199	-265	-66	-15	4	9	0	-18	429	-420
Seasonal AWS-L (W m⁻²)														
Winter	196	-113	83	0.58	178	-247	-69	-26	13	5	0	-2	392	-388
Pre-monsoon	287	-200	87	0.70	223	-275	-52	-16	1	5	0	-22	517	-513
Monsoon	201	-113	88	0.56	302	-307	-5	-1	1	-3	0	-66	504	-490
Post-monsoon	235	-108	127	0.46	205	-273	-68	-18	4	6	0	-33	450	-432
Seasonal AWS-H (W m⁻²)														
Winter	183	-120	63	0.66	167	-231	-63	-19	15	3	0	0	368	-369
Pre-monsoon	280	-204	76	0.73	212	-265	-52	-17	1	4	0	-13	496	-498
Monsoon	198	-155	43	0.78	291	-305	-13	-4	-1	5	0	-29	494	-493
Post-monsoon	221	-146	75	0.66	195	-261	-66	-15	4	10	0	-12	430	-433

1138 **Table 6.** Glacier-wide annual and seasonal mass balance components (mm w.e.) over the total glacier area and at point scale at

1139 AWS-L and AWS-H using all data over the study period 2016-20. The negative (-) sign indicates a mass loss from the surface.

	Snowfall	Sublimation	Surface melt	Subsurface melt	Total melt	Refreezing	Mass balance
Annual means (mm w.e.)							
Glacier-wide mean	718	-150	-2095	-88	-2183	956	-656
AWS-L	641	-164	-3194	-88	-3282	659	-2144
AWS-H	792	-149	-1434	-88	-1522	1174	297
Seasonal Glacier-wide (mm w.e.)							
Winter	77	-62	-43	-4	-47	27	-4
Pre-monsoon	137	-48	-395	-20	-415	298	-27
Monsoon	479	-10	-1366	-53	-1419	489	-461
Post-monsoon	25	-30	-291	-11	-302	142	-165
Seasonal AWS-L (mm w.e.)							
Winter	77	-74	-51	-6	-57	41	-12

Pre-monsoon	136	-50	-519	-29	-548	368	-94
Monsoon	403	-4	-2098	-47	-2145	191	-1554
Post-monsoon	25	-36	-526	-6	-532	58	-485
Seasonal AWS-H (mm w.e.)							
Winter	77	-54	-11	-1	-12	11	22
Pre-monsoon	138	-51	-309	-17	-326	275	37
Monsoon	551	-15	-929	-57	-986	701	251
Post-monsoon	26	-29	-185	-12	-197	187	-13

1140 **Table 7.** Mass balance anomalies as compared to the mean of the four 2016-20 years from the classical and synthetic scenarios'
1141 methods.

Sensitivity	Classical method (m w.e.)	Synthetic scenarios (m w.e.)
-1 °C T	+0.41	+0.93 ± 0.18
+1 °C T	-0.61	-0.75 ± 0.17
+20 % P	+0.48	+0.52 ± 0.10
-20 % P	-0.79	-0.60 ± 0.11

1142
1143 **Table 8.** Comparison of SEB components on different glaciers in HMA, whose location is visible in Fig. S18. The various studies
1144 already included in Azam and others (2014) are not reported in this table. (All the fluxes are in $W m^{-2}$)

Glacier Name	Study type	Altitude (m a.s.l.)	Region (ISM dominated, Y or N)	Study Period	SW net	LW net	QS	QL	QC	QM	Reference
Parlung No. 4	Point/annual	4657-5937	southeast Tibetan Plateau, China (N)	1 Oct 2008 to 21 Sept 2013	77	-46	11	-21	1	-22	Zhu and others (2018)
Zhandang	Point/annual	5515-5947	western Nyainqen Tanglha Range, China (Y)	1 Oct 2008 to 21 Sept 2013	69	-49	14	-13	-1	-20	Zhu and others (2018)
Purogangri ice cap	Glacier	5350-6370	Tibetan Plateau,	Oct 2000 to	36	-39	28	-22	-1.3	-2	Huintjes and others (2015)

	wide/ annual		China (Y)	Oct 2011							
Qiangtang No.1	Point/ annual	5882	inland Tibetan Plateau, China (Y)	Oct 2012 to Oct 2016	49	-56	26	- 15	2	-6	Li and others (2018)
Rikha Samba	Glacie r- wide/ annual	5427- 6515	Central Himalay a, Nepal (Y)	Oct 1974 to Sept 2021	105	-74	- 20 *		NA	-12	Gurung and others (2022)
Naimona'nyi	Glacie r- wide/ annual	5545- 7262	western Himalay a, China (Y)	Oct 2010 to Sept 2018	77	-69	12	- 16	2	6	Zhu and others (2021)
Dokriani	Glacie r- wide/ annual	4050- 6632	western Himalay a, India (Y)	1979 to 2020	68	-35	9	- 32	NA	-10	Srivastava and Azam (2022)
Chhota Shigri	Point/ monso on	4670	western Himalay a, India (Y)	8 Jul to 5 Sept 2013	202	-14	31	11	4	- 233	Azam, and others (2014)
Chhota Shigri	Glacie r- wide/ annual	4070- 5850	western Himalay a, India (Y)	1979 to 2020	77	-57	15	- 25	NA	-10	Srivastava and Azam (2022)
Srutri Dhaka	Glacie r- wide/ annual	4500- 6000	western Himalay a, India (Y)	Oct 2015 to Sept 2017	157	-85	7	-5	-3	-71	Oulkar and others (2022)
Muztag Ata No. 15	Point/ annual	5237- 5935	eastern Pamir, China (N)	1 Oct 2008 to 21 Sept 2013	69	-61	18	- 24	0	-2	Zhu and others (2018)

1145 *corresponding to QS+QL here

1146

1147

1148 **Supplementary material of “Surface energy and mass balance of Mera Glacier (Nepal, Central Himalaya)**
 1149 **and their sensitivity to temperature and precipitation”** by Arbindra Khadka, Fanny Brun, Patrick Wagnon,
 1150 Dibas Shrestha, Tenzing Chogyal Sherpa

1151
 1152 *Table S1. Monthly correlation coefficients (r^2) between the Mera La AWS and AWS-L hourly data with parameters used to linearly*
 1153 *extrapolate the Mera La AWS data to AWS-L ($y = mx + c$). For SWin, the c value is 0 i.e., the correlation is forced to the origin, in*
 1154 *order to keep night values at 0 W m⁻².*

Variables	T			RH			u			SWin			LWin		
	r ²	m	c	r ²	m	c	r ²	m	c	r ²	m	c	r ²	m	C
all	0.92	0.90	-2.09	0.91	0.94	5.47	0.51	0.94	0.70	0.90	1.10	0	0.93	0.92	12.77
Jan	0.86	0.86	-3.07	0.82	0.86	4.94	0.41	0.80	1.62	0.95	0.93	0	0.77	0.77	37.72
Feb	0.90	0.86	-2.82	0.85	0.89	3.60	0.45	0.69	1.88	0.97	0.98	0	0.88	0.84	27.90
Mar	0.88	0.82	-2.83	0.79	0.87	3.28	0.37	0.79	1.61	0.96	1.08	0	0.82	0.78	38.44
Apr	0.81	0.72	-3.06	0.81	0.91	3.98	0.34	0.79	1.16	0.91	1.23	0	0.71	0.76	44.96
May	0.73	0.66	-2.19	0.78	0.93	3.73	0.22	0.64	1.31	0.87	1.26	0	0.73	0.81	37.50
Jun	0.65	0.59	-0.90	0.72	0.84	15.59	0.26	0.69	0.53	0.83	1.32	0	0.76	0.88	29.04
Jul	0.65	0.45	-0.10	0.31	0.45	53.71	0.09	0.49	0.55	0.83	1.27	0	0.61	0.78	64.50
Aug	0.64	0.44	-0.14	0.42	0.54	44.88	0.15	0.61	0.48	0.81	1.22	0	0.76	0.86	37.92
Sep	0.70	0.61	-1.03	0.64	0.72	28.11	0.15	0.45	0.55	0.84	1.15	0	0.78	0.97	1.67
Oct	0.80	0.79	-2.95	0.81	0.89	10.95	0.19	0.61	1.05	0.91	1.05	0	0.86	0.86	26.36
Nov	0.79	0.77	-3.53	0.74	0.81	10.53	0.25	0.59	1.75	0.95	0.96	0	0.83	0.80	35.77
Dec	0.89	0.84	-3.12	0.77	0.85	8.55	0.47	0.77	1.59	0.96	0.93	0	0.85	0.84	26.40

1155
 1156 *Table S2. Tested range and final values of the altitudinal gradients of air temperature, relative humidity, incoming longwave*
 1157 *radiation and precipitation used to spatially distribute the meteorological forcing data*

SN	Parameters	Max	Min	final value
1	Temperature gradient (°C km ⁻¹)	-4.2	-6.5	-5.7
2	Relative humidity gradient (% km ⁻¹)	0	-20	-15
3	LWin gradient (W m ⁻² km ⁻¹)	0	-41	-25
4	Precipitation gradient (mm km ⁻¹ or % km ⁻¹)			0

1158
 1159
 1160

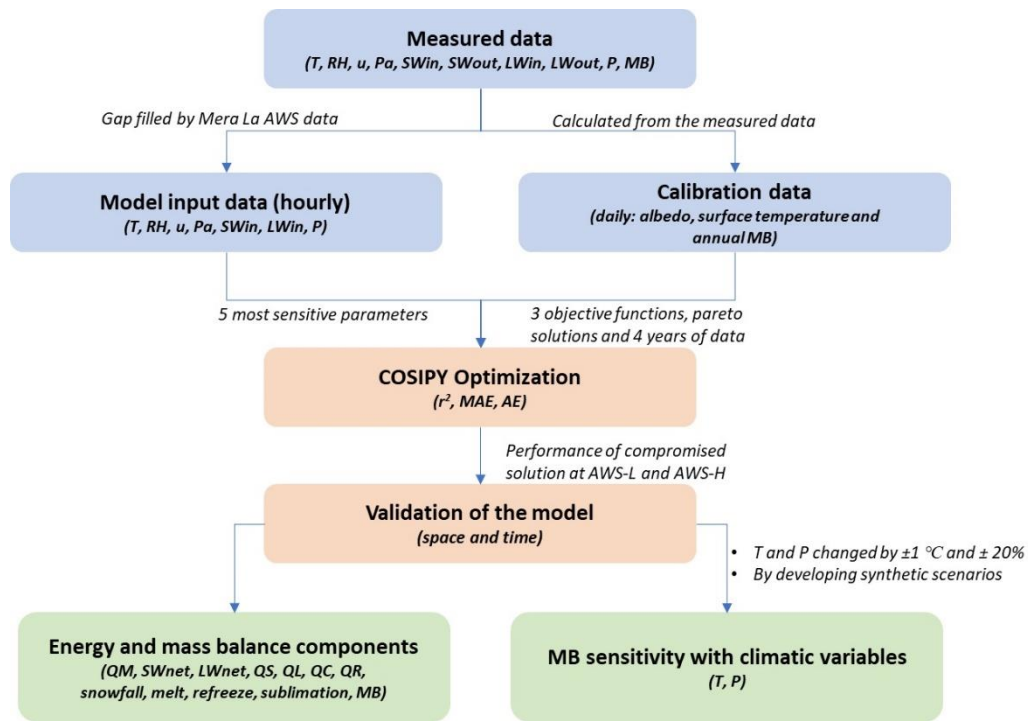
1161 Table S3. Glacier-wide annual mass balance perturbations (m w.e.) with different magnitudes of meteorological variables from
 1162 various studies done on HMA glaciers, always using the classical method, except our present study using the synthetic scenario
 1163 approach. (* refers to the sensitivities obtained from the literature, but multiplied or divided by a factor to make it comparable
 1164 with other studies. For example, the mass balance sensitivity to a -10 % change in precipitation is multiplied by a factor 2, to make
 1165 it comparable with a mass balance sensitivity to a -20 % change in precipitation.)

Glacier Name, region	Region (ISM dominated, Y or N)	Study Period	T (-1 °C)	T (+1 °C)	P (-20 %)	P (+20 %)	Reference
Parlung No 4	southeast Tibetan Plateau, China (N)	1 Oct 2008 to 21 Sept 2013	+1.28	-1.28	-0.29	+0.29	Zhu and others (2018)
Parlung No 4	southeast Tibetan Plateau, China (N)	Oct 2000 to Sept 2018	+0.44	-0.55	-0.86	+0.51	Arndt and Schneider (2023)
Parlung No 94	southeast Tibetan Plateau, China (N)	Oct 2000 to Sept 2018	+1.03	-1.14	-1.56	+0.89	Arndt and Schneider (2023)
Zhadang	western Nyainqentanglha Range, China (Y)	1 Oct 2008 to 21 Sept 2013	+1.30	-1.30	-0.52	+0.52	Zhu and others (2018)
Zhadang	western Nyainqentanglha Range, China (Y)	Oct 2000 to Sept 2018	+1.68	-2.96	-2.34	+1.57	Arndt and Schneider (2023)
Mera	Central Himalaya, Nepal (Y)	Nov 2016 to Oct 2020	+0.93	-0.75	-0.60	+0.52	Present study
Trambau	Central Himalaya, Nepal (Y)	May 2016 to Oct 2018	NA	-0.90*	NA	+0.36*	Sunako and others (2019)
Yala	Central Himalaya, Nepal (Y)	Oct 2000 to Sept 2018	+1.65	-3.18	-2.19	+1.25	Arndt and Schneider (2023)
Rikha Samba	Central Himalaya, Nepal (Y)	Oct 1974 to Sept 2021	+0.54	-0.69	-0.44	+0.35	Gurung and others (2022)

Halji	Central Himalaya, Nepal (Y)	Oct 2000 to Sept 2018	+1.22	-1.33	-1.53	+1.07	Arndt and Schneider (2023)
Halji	Central Himalaya, Nepal (Y)	Jan 1982 to Apr 2019	+0.99	-1.43	-1.29	+0.76	Arndt and others (2021)
Naimona'nyi	Central Himalaya, Nepal (Y)	Oct 2000 to Sept 2018	+0.47	-1.8	-1.46	+0.49	Arndt and Schneider (2023)
Naimona'nyi	western Himalaya, India (Y)	Oct 2010 to Sept 2018	+0.37	-0.37	-0.20*	+0.20*	Zhu and others (2021)
Dokriani	western Himalaya, India (Y)	Nov 1979 to Oct 2020	+0.50	-0.50	-0.46	+0.46*	Srivastava and Azam (2022)
Chhota Shigri	western Himalaya, India (Y)	Nov 1979 to Oct 2020	+0.30	-0.30	-0.26	+0.26*	Srivastava and Azam (2022)
Chhota Shigri	western Himalaya, India (Y)	Oct 2000 to Sept 2018	+0.49	-0.53	-0.67	+0.53	Arndt and Schneider (2023)
Shruti Dhaka	western Himalaya, India (Y)	Oct 2015 to Sept 2017	+0.15	-0.25	-0.34*	+0.42*	Oulkar and others (2022)

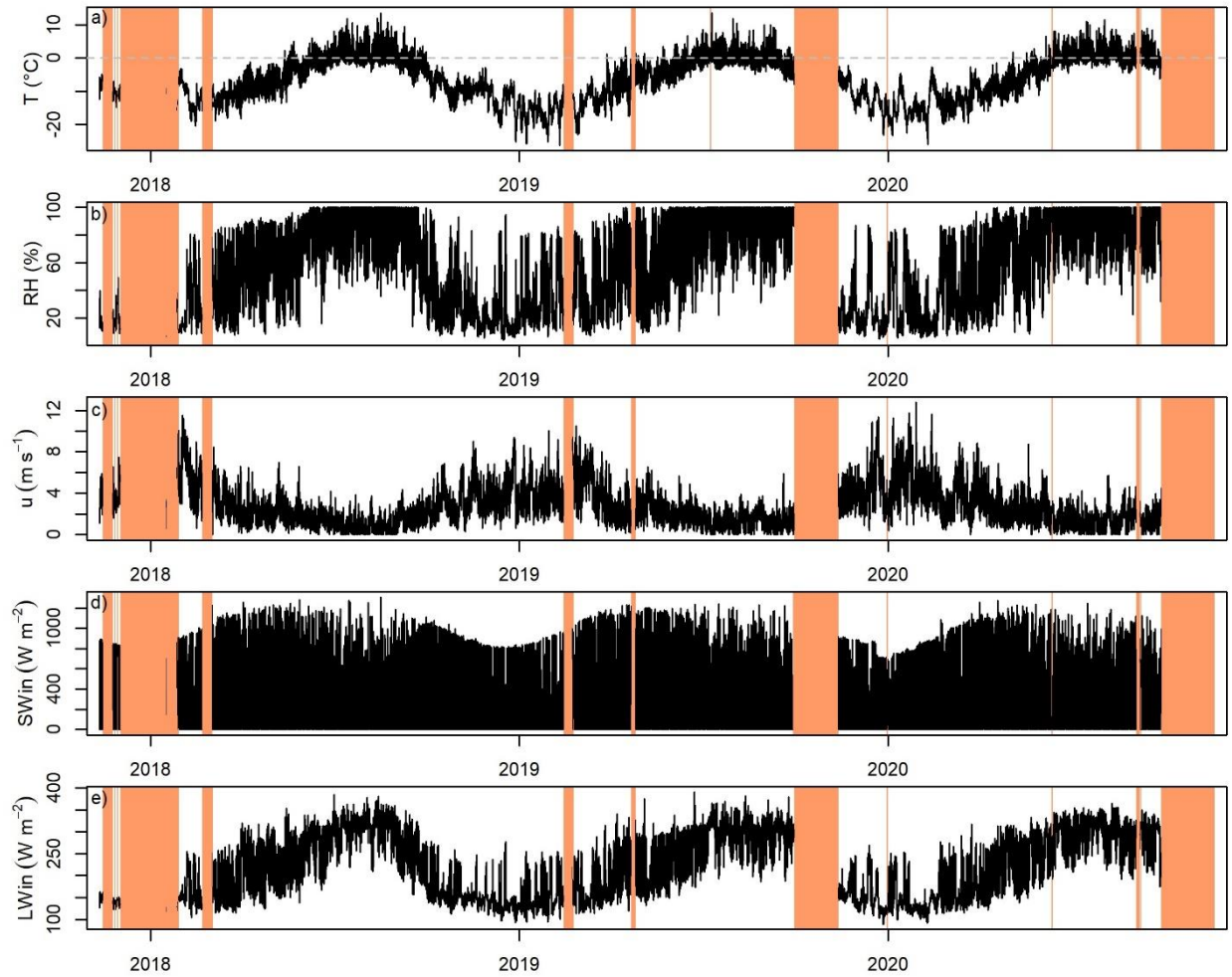
1166

1167



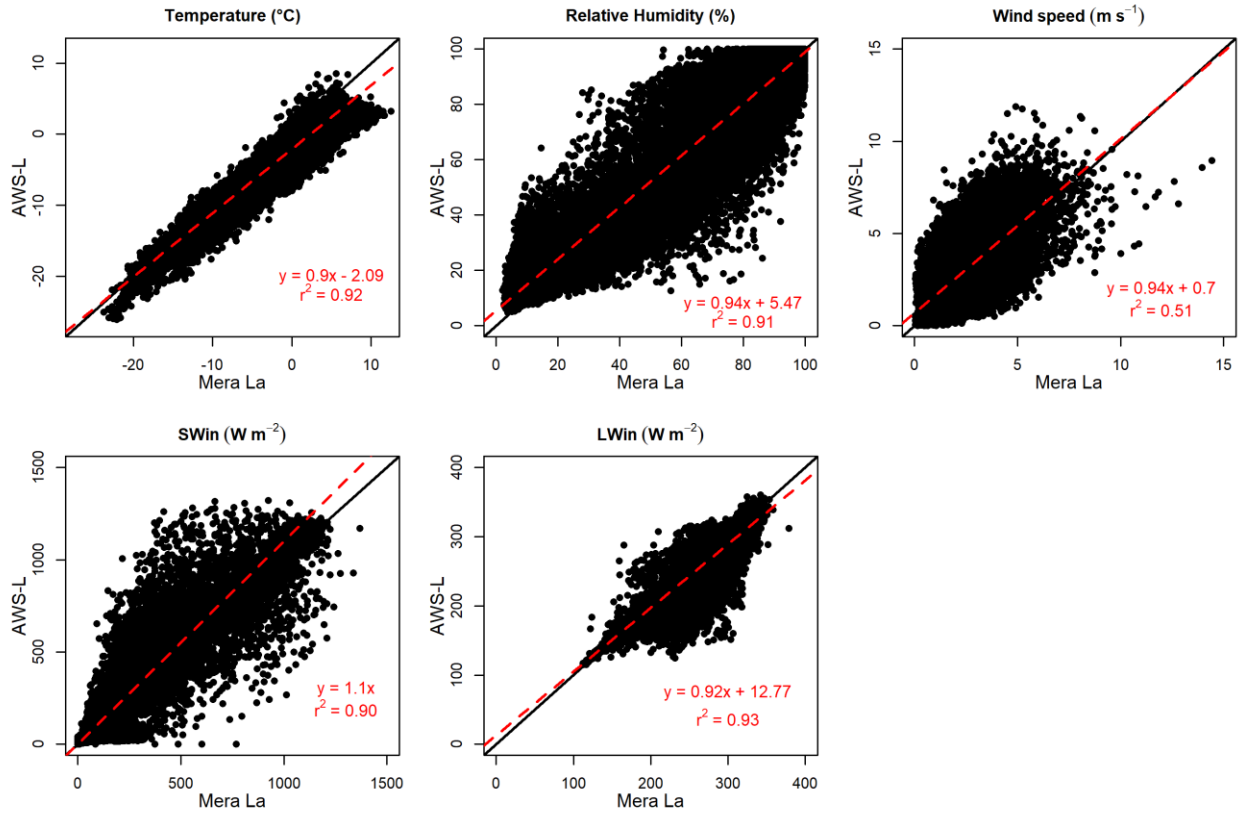
1168
1169
1170
1171

Figure S1. Flow chart describing the simplified sequential approach used in this study.

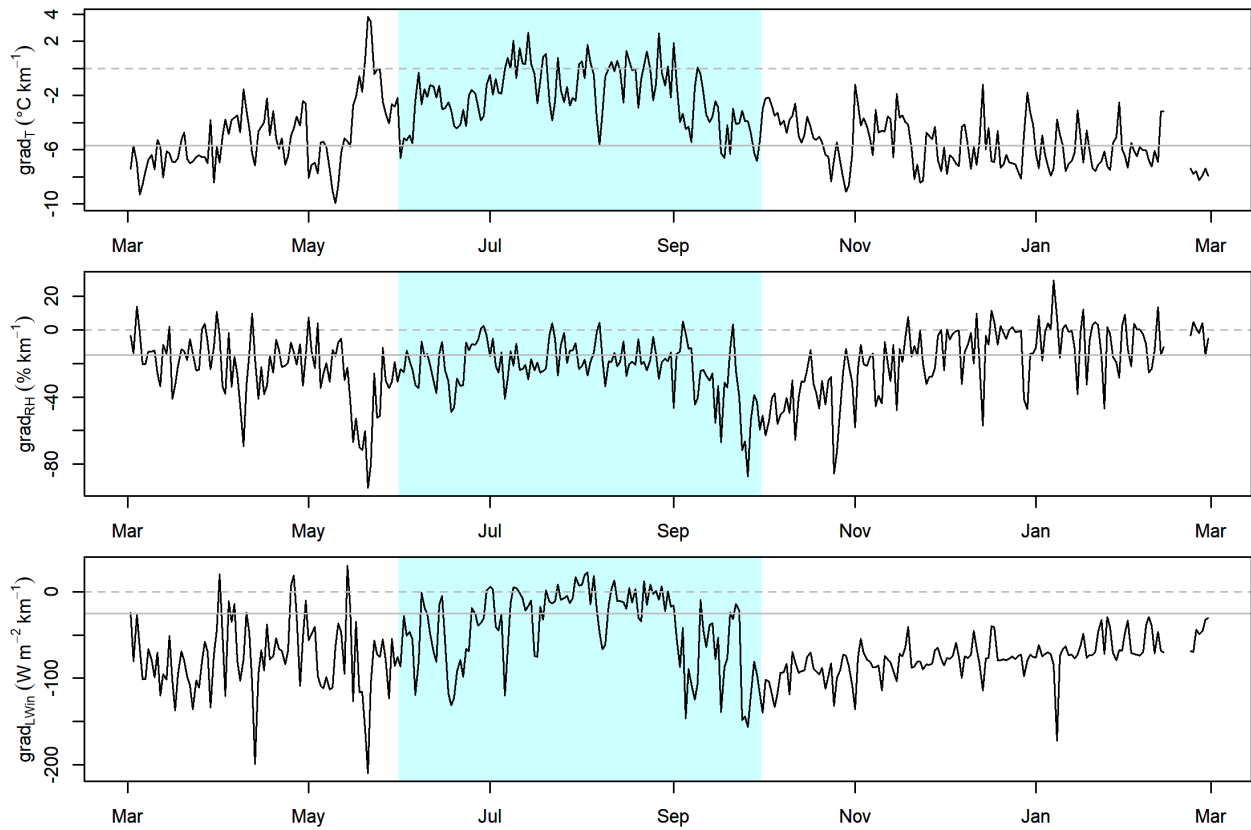


1172
 1173 *Figure S2. Hourly data of (a) air temperature (T), (b) relative humidity (RH), (c) wind speed (u), (d) incoming shortwave radiation*
 1174 *($SWin$), and (e) incoming longwave radiation ($LWin$) at AWS-H, from 10 November 2017 to 27 September 2020. Orange shaded*
 1175 *areas indicate data gaps.*

1176



1177
 1178 *Figure S3. Hourly data comparison between Mera La and AWS-L. The red lines and equations are overall linear relationships*
 1179 *between the two observed data, r^2 is the correlation coefficient, where the p-value is always significant ($p < 0.01$). Also shown in*
 1180 *black the 1:1 line.*



1181
 1182 *Figure S4. Mean daily altitudinal gradients of air temperature ($grad_T$), relative humidity ($grad_{RH}$), and longwave incoming radiation*
 1183 *($grad_{LWin}$), calculated from AWS-L and AWS-H data from 1 March 2018 to 28 February 2019. The horizontal grey lines represent*
 1184 *the different values of altitudinal gradients used for the data distribution. The blue shaded area corresponds to the monsoon*
 1185 *period.*

1186

1187 **Additional text related to fig. S4: Pressure data distribution method, altitudinal gradients of air**
1188 **temperature, relative humidity and incoming longwave radiation used in this study**

1189 The atmospheric pressure (Pa) has been interpolated using the barometric formula (eq. S1, S2):

$$SLP = \frac{Pa}{\left(1 - \frac{(0.0065 * Z_{AWS-L})}{288.15}\right)^{5.255}} \quad (S1)$$

$$Pa_{elv} = SLP * \left(1 - \frac{0.0065 * Z_{elv}}{288.15}\right)^{5.255} \quad (S2)$$

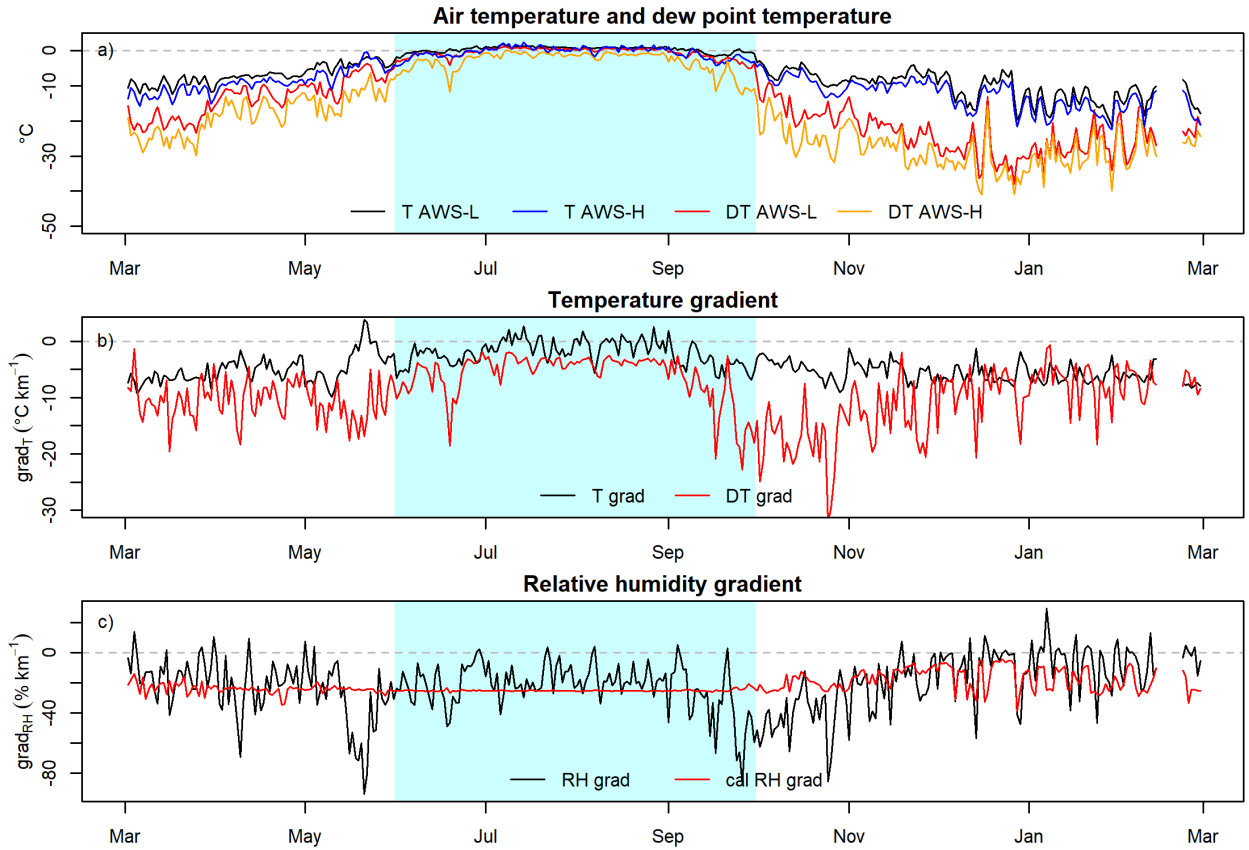
1190 Where SLP is the sea level pressure, Pa is the atmospheric pressure at the elevation of the AWS-L
1191 (Z_{AWS-L}), and Pa_{elv} is the pressure at any grid elevation (Z_{elv}).

1192

1193 The altitudinal gradients of air temperature, relative humidity and incoming longwave radiation are
1194 calculated using the data from AWS-L and AWS-H between 01 March 2018 and 28 February 2019. This
1195 particular period is chosen because there are almost no gaps at AWS-H (Fig. S1) and because it covers one
1196 full year, allowing to compute annual and seasonal gradients. However, it is worth noting that during this
1197 period, a large portion of data at AWS-L (from 01 March 2018 to 24 November 2018) has been
1198 reconstructed with Mera La AWS. Using reconstructed data does not alter our analysis since we explore
1199 different gradients over a wide range of values. For air temperature, this range goes from the
1200 environmental lapse rate ($-6.5 \text{ }^\circ\text{C km}^{-1}$) to the mean annual temperature gradient observed from both
1201 AWSs ($-0.42 \text{ }^\circ\text{C km}^{-1}$). For the other variables, the range goes from the mean monsoonal observed gradient
1202 ($-22 \text{ } \%$ km^{-1} and $-41 \text{ Wm}^{-2} \text{ km}^{-1}$ for RH and LW in gradients, respectively) to 0 (no gradient) (Fig. S3). Deriving
1203 dew point temperature gradients between AWS and converting dew point temperature to relative
1204 humidity at any glacier grid cell is more physical than directly using relative humidity gradients, but both
1205 approaches provide the same range of RH gradients (Fig. S4). Twelve tests were conducted with different
1206 sets of gradients to ultimately determine the optimal set, which is $-5.7 \text{ }^\circ\text{C km}^{-1}$ for air temperature, $-15 \text{ } \%$
1207 km^{-1} for relative humidity and $-25 \text{ W m}^{-2} \text{ km}^{-1}$ for incoming longwave radiation (Table S2).

1208

1209
1210



1211

1212 *Figure S5. Mean daily temperature (T) and dew point temperature (DT) at AWS-L and AWS-H (top), calculated temperature and*
1213 *dew point temperature gradient (middle) and calculated relative humidity gradient from observation and dew point temperature*
1214 *(bottom) from the AWS-L and AWS-H from 1 March 2018 to 28 February 2019.*

1215

1216 Additional text related to the method section

1217 Albedo

1218 In COSIPY, the albedo (α) of the snow surface is calculated by the Oerlemans and Knap (1998) method.
1219 The albedo of snow (α_{sn}) depends upon how fast (t^* expressed in days) the fresh snow albedo (α_s) drops
1220 to firn albedo (α_f) after the last snowfall.

$$\alpha_{sn} = \alpha_f + (\alpha_s - \alpha_f) \exp\left(-\frac{t}{t^*}\right) \quad (S3)$$

1221 where s is the age of the snow layer from the last snowfall (in days). The overall snowpack thickness (d in
 1222 m) impacts the albedo; if the snowpack is thin, the albedo must tend towards the albedo of ice (α_i). The
 1223 full albedo can be written by introducing a characteristic snow depth scale d^* (in m) as

$$\alpha = \alpha_{sn} + (\alpha_i - \alpha_{sn}) \exp\left(\frac{-d}{d^*}\right) \quad (S4)$$

1224 **Densification**

1225 The snow volumetric mass (ρ_{sn} in kg m^{-3}) is a key characteristic of the snowpack. Following Essery and
 1226 others (2013), COSIPY calculates the snow volumetric mass to derive important snow properties such as
 1227 thermal conductivity and liquid water content. Assuming that a rapid settlement of fresh snow occurs
 1228 simultaneously with slow compaction by the load resisted by the viscosity (η), the rate of change in the
 1229 volumetric mass as a function of time t , $\frac{d\rho_{sn}}{dt}$, of a snow layer with temperature T_{sn} and overlying mass
 1230 M_{sn} is given by:

$$\frac{1}{\rho_{sn}} \frac{d\rho_{sn}}{dt} = \frac{M_{sn}g}{\eta} + c_1 \exp[-c_2(T_0 - T_{sn}) - c_3 \max(0, \rho_{sn} - \rho_0)] \quad (S5)$$

1231 And the viscosity:

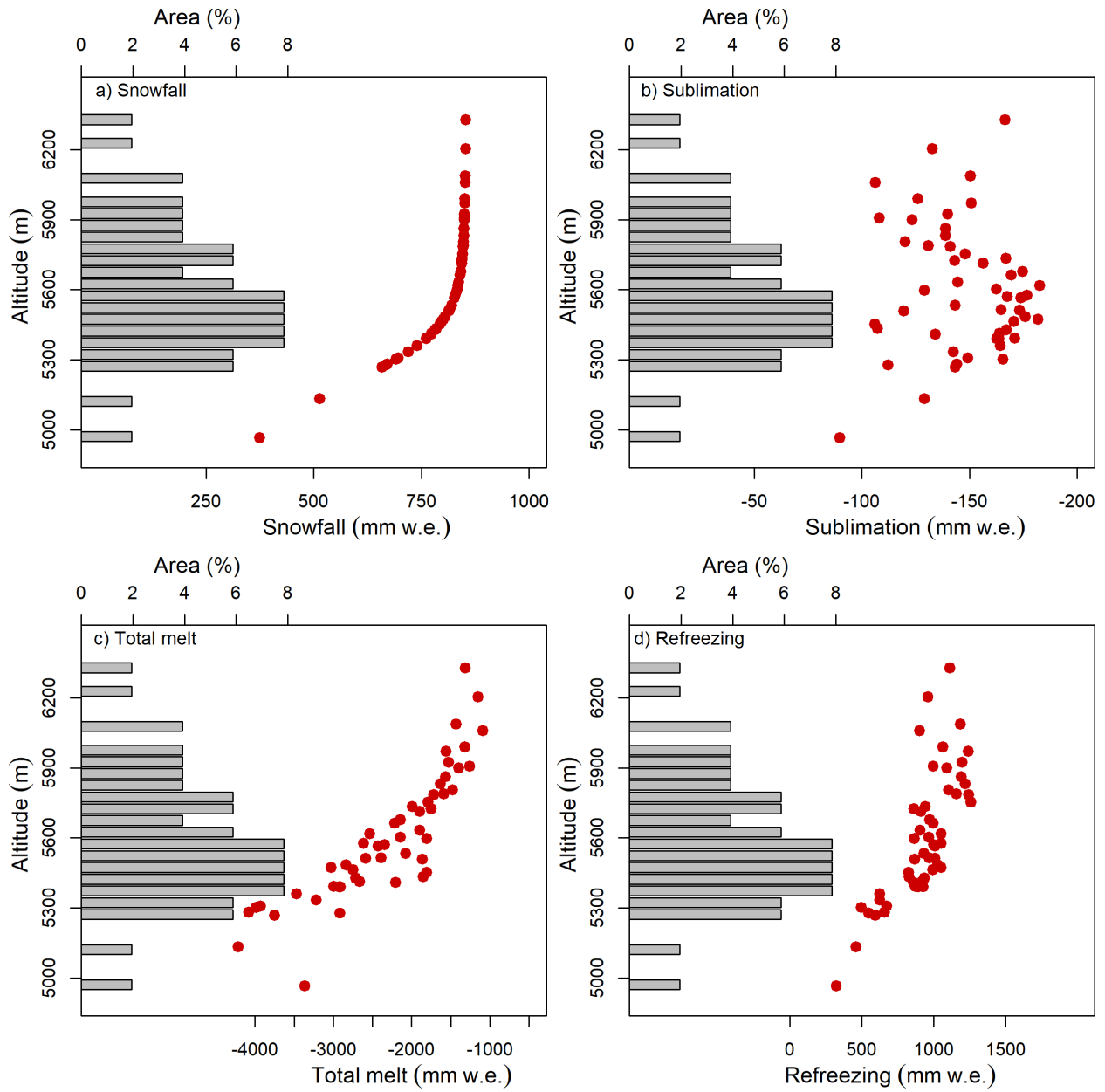
$$\eta = \eta_0 \exp[c_4(T_0 - T_{sn}) + c_5 \rho_{sn}] \quad (S6)$$

1232 Values for the two physical constants and six parameters in equations (S3) and (S4) are given in Table S4
 1233 below.

1234 **Table S4.** Physical constants and parameter values for snow compaction parameterisations
 1235

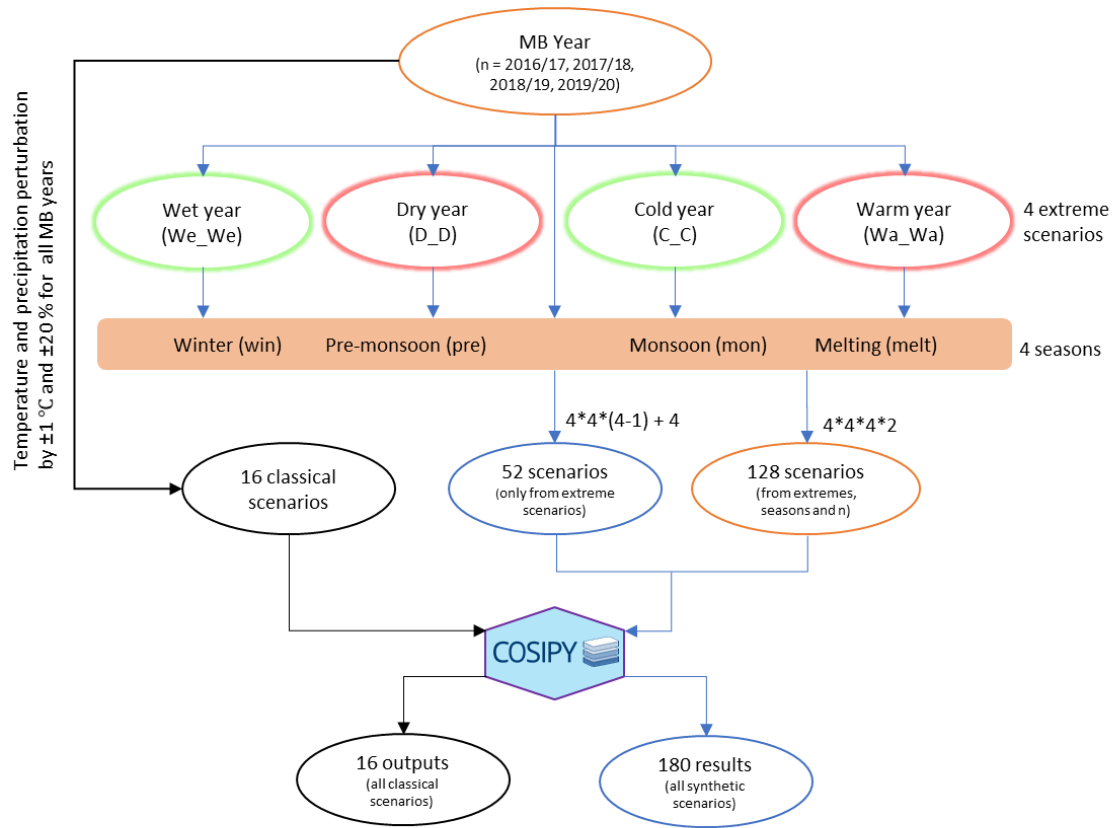
equation	Parameters	Sources
S5	$c_1 = 2.8 \times 10^{-6} \text{ s}^{-1}$, $c_2 = 0.042 \text{ K}^{-1}$, $c_3 = 0.046 \text{ m}^3 \text{ kg}^{-1}$ $\rho_0 = 150 \text{ kg m}^{-3}$ $T_0 = 273.15 \text{ K}$ melting point temperature $g = 9.81 \text{ m s}^{-2}$ acceleration due to gravity	(Anderson, 1976; Boone, 2002; Essery and others, 2013; Sauter and others, 2020)
S6	$c_4 = 0.081 \text{ K}^{-1}$ $c_5 = 0.018 \text{ m}^3 \text{ kg}^{-1}$ $\eta_0 = 3.7 \times 10^7 \text{ kg m}^{-1} \text{ s}^{-1}$	

1236
 1237



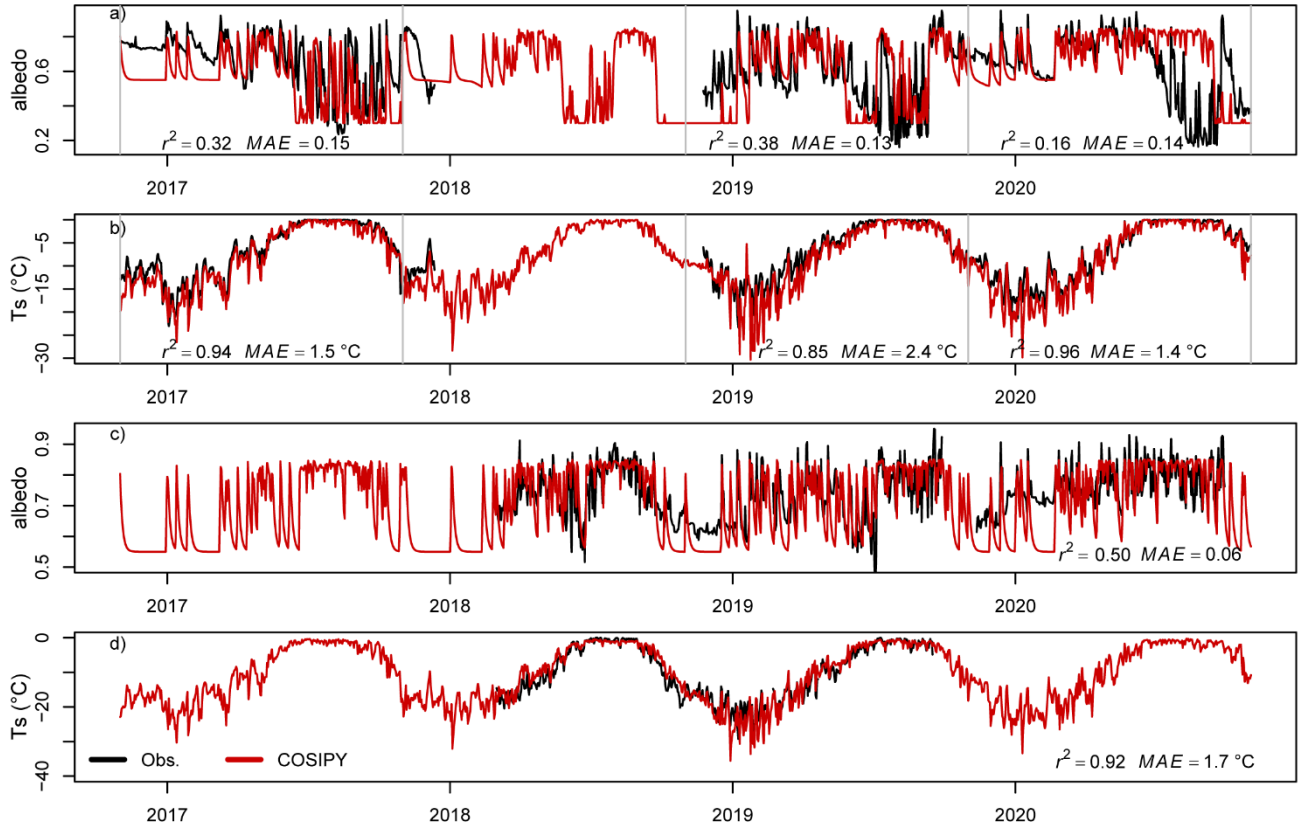
1238
 1239 *Figure S6. Total (a) snowfall, (b) sublimation, (c) melt and (d) refreezing (red dots) for each grid cell simulated by COSIPY for the*
 1240 *2018/19 period. Also shown is the glacier hypsometry (grey histograms) used in the model.*

1241



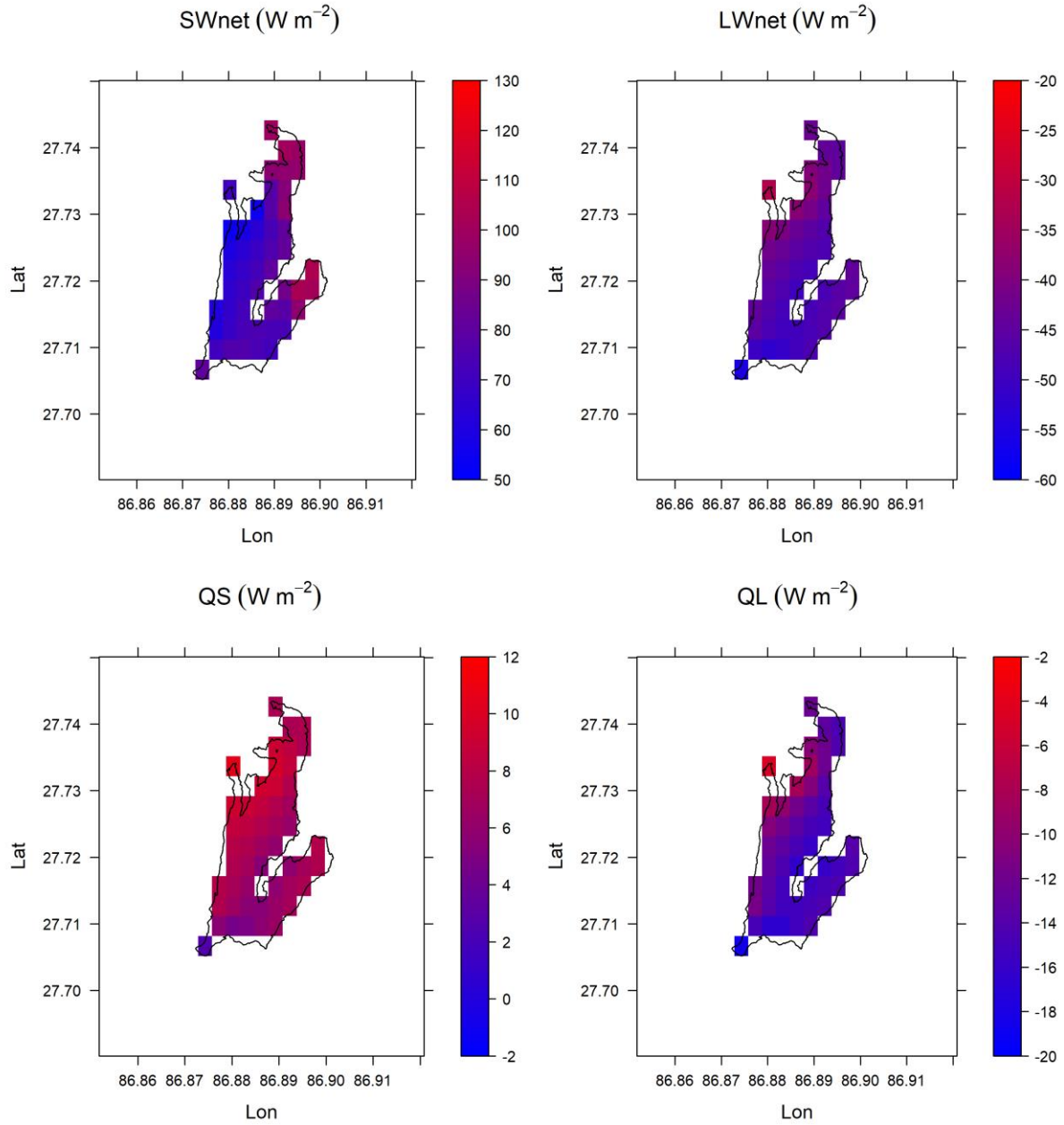
With mean, 4 results from classical scenarios, 180 results from synthetic scenarios

1242
 1243 *Figure S7. Flow chart illustrating the sequential approach used to develop and analyse mass balance sensitivity by both classical*
 1244 *and synthetic methods.*
 1245

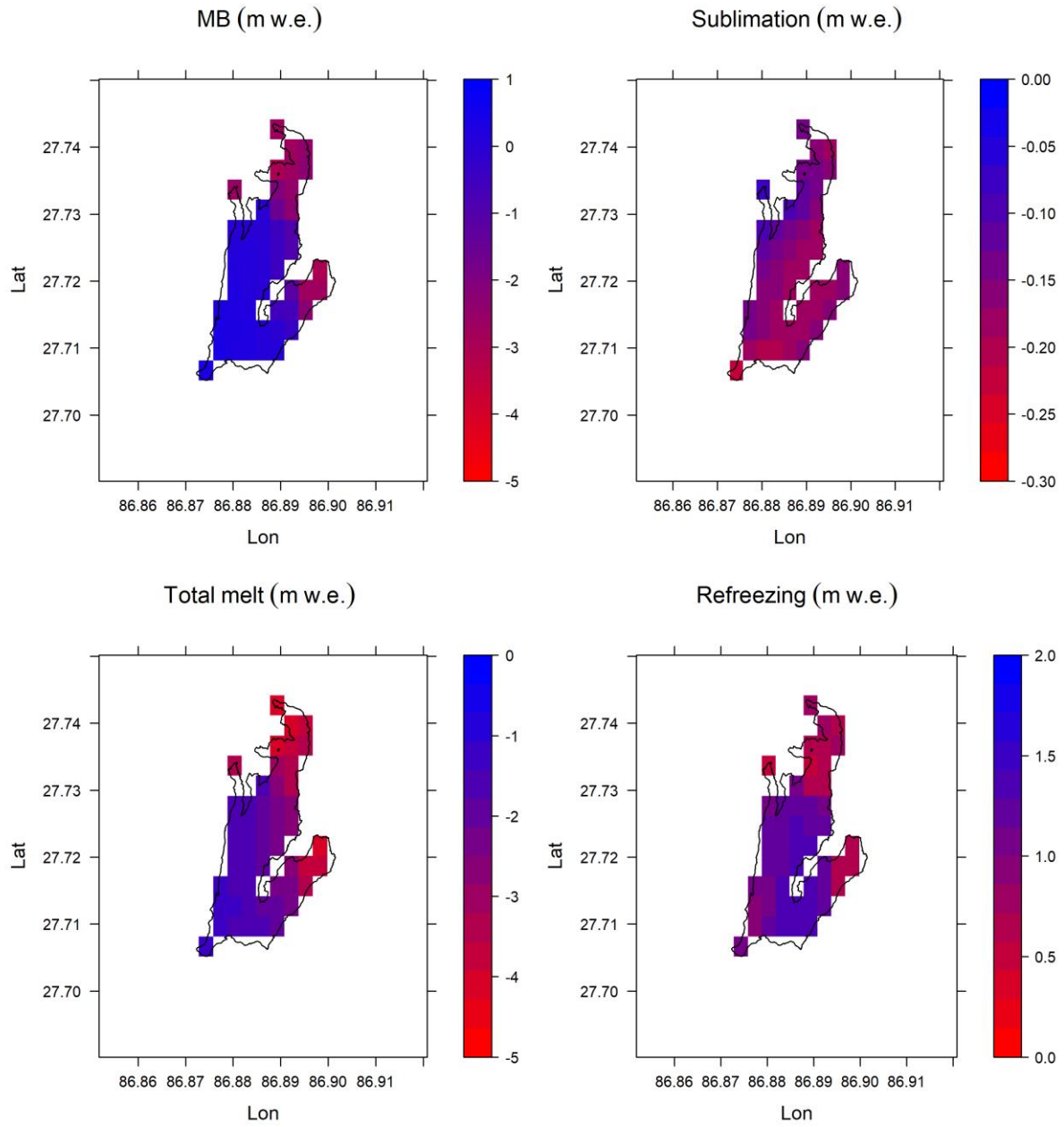


1246
 1247 *Figure S8. Mean daily observed and modelled albedo and surface temperature at AWS-L (a and b) and AWS-H (c and d) for the*
 1248 *2016-20 period. The metrics r^2 and MAE are calculated for each year at AWS-L (except 2017/18, because the data gap is too long)*
 1249 *and for the 3-year 2017-20 period at AWS-H.*

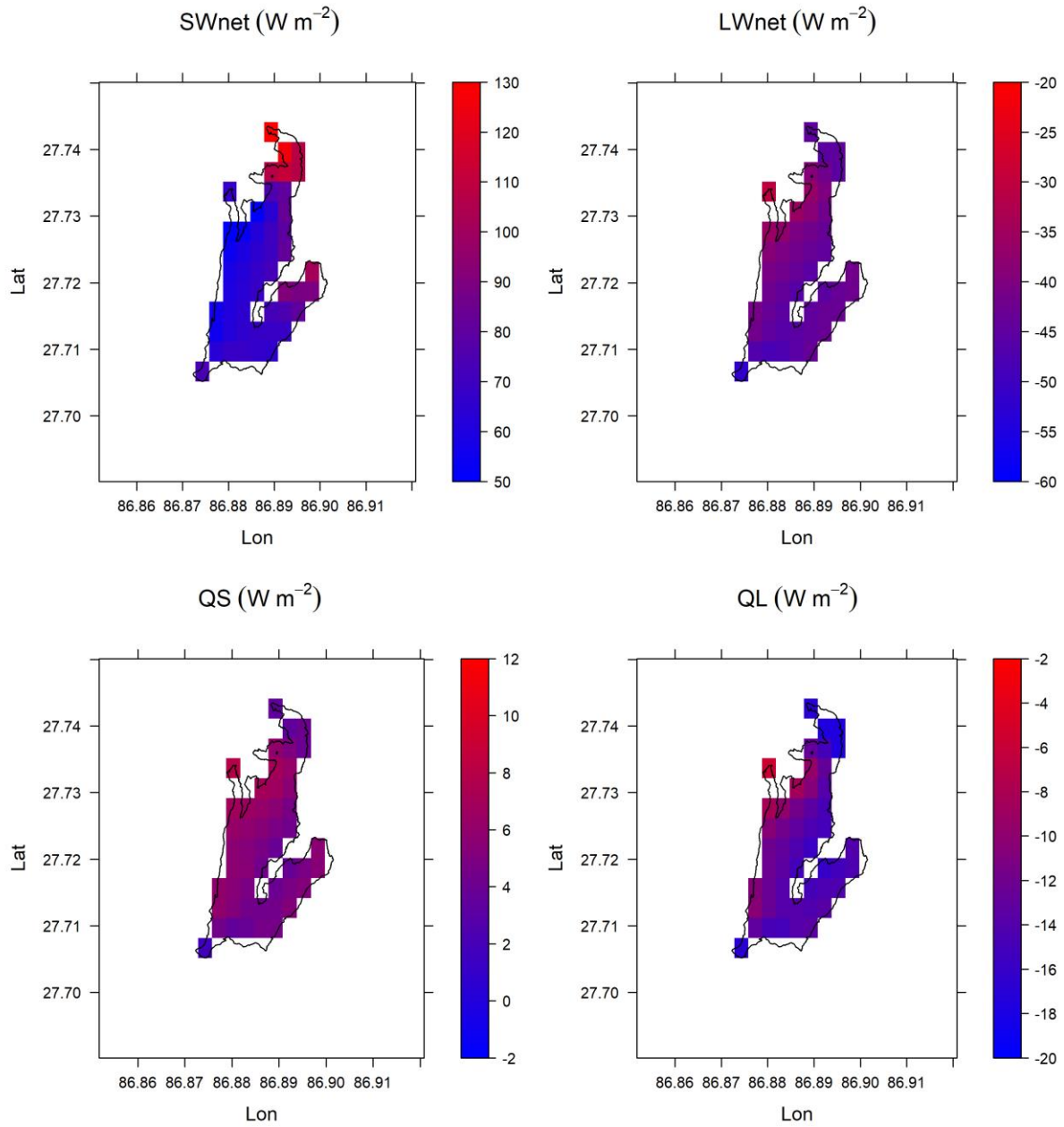
1250



1251
 1252 *Figure S9. Distributed annual net shortwave radiation (SWnet), net longwave radiation (LWnet), sensible heat flux (QS), and*
 1253 *latent heat flux (QL) in $W m^{-2}$ for the year 2016/17. The glacier outlines (black) is from Wangno and others (2021).*
 1254

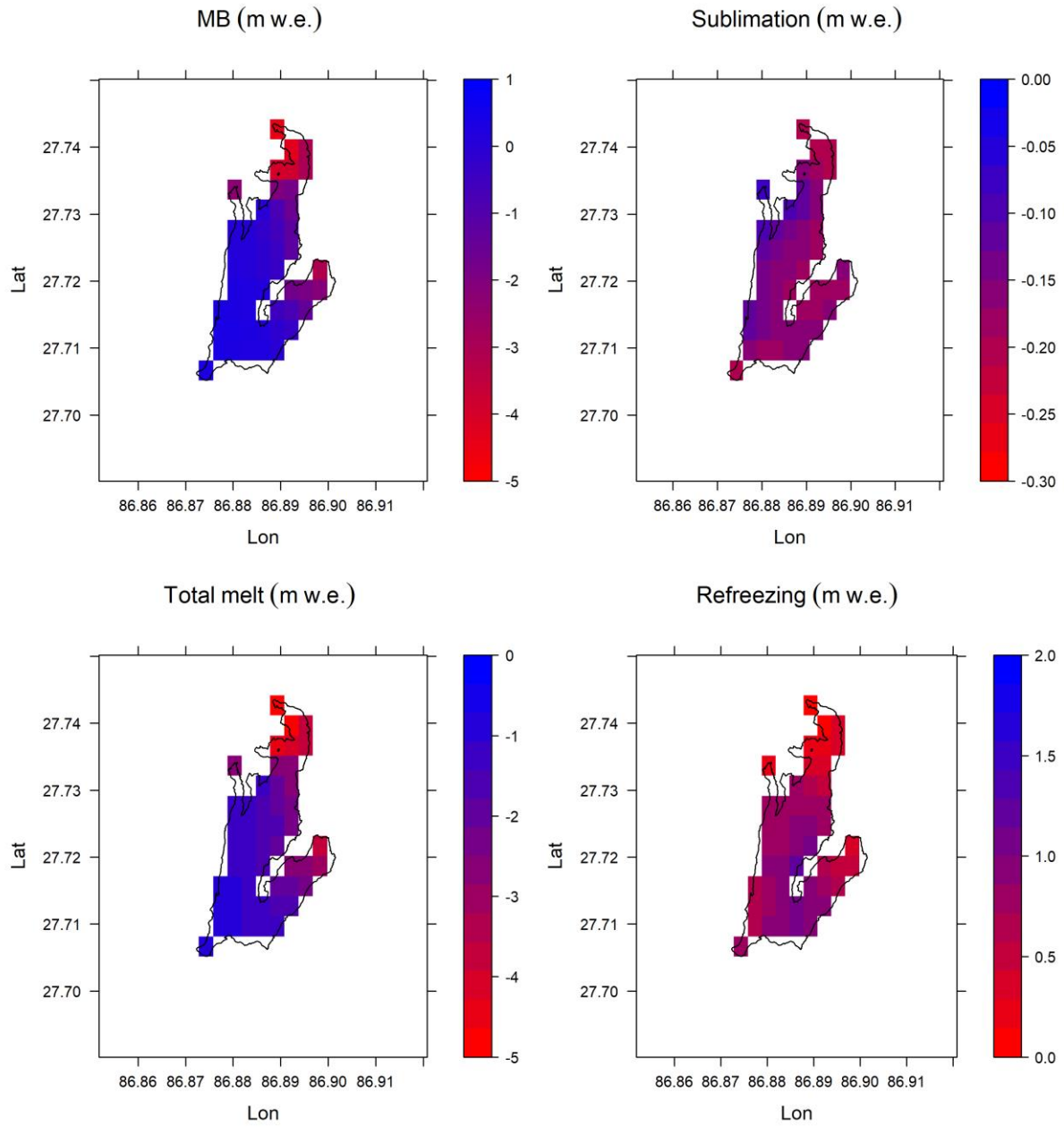


1255
 1256 *Figure S10. Distributed annual mass balance (MB), sublimation, total melt and refreezing in m w.e. for the year 2016/17. The*
 1257 *glacier outlines (black) is from Wangno and others (2021).*

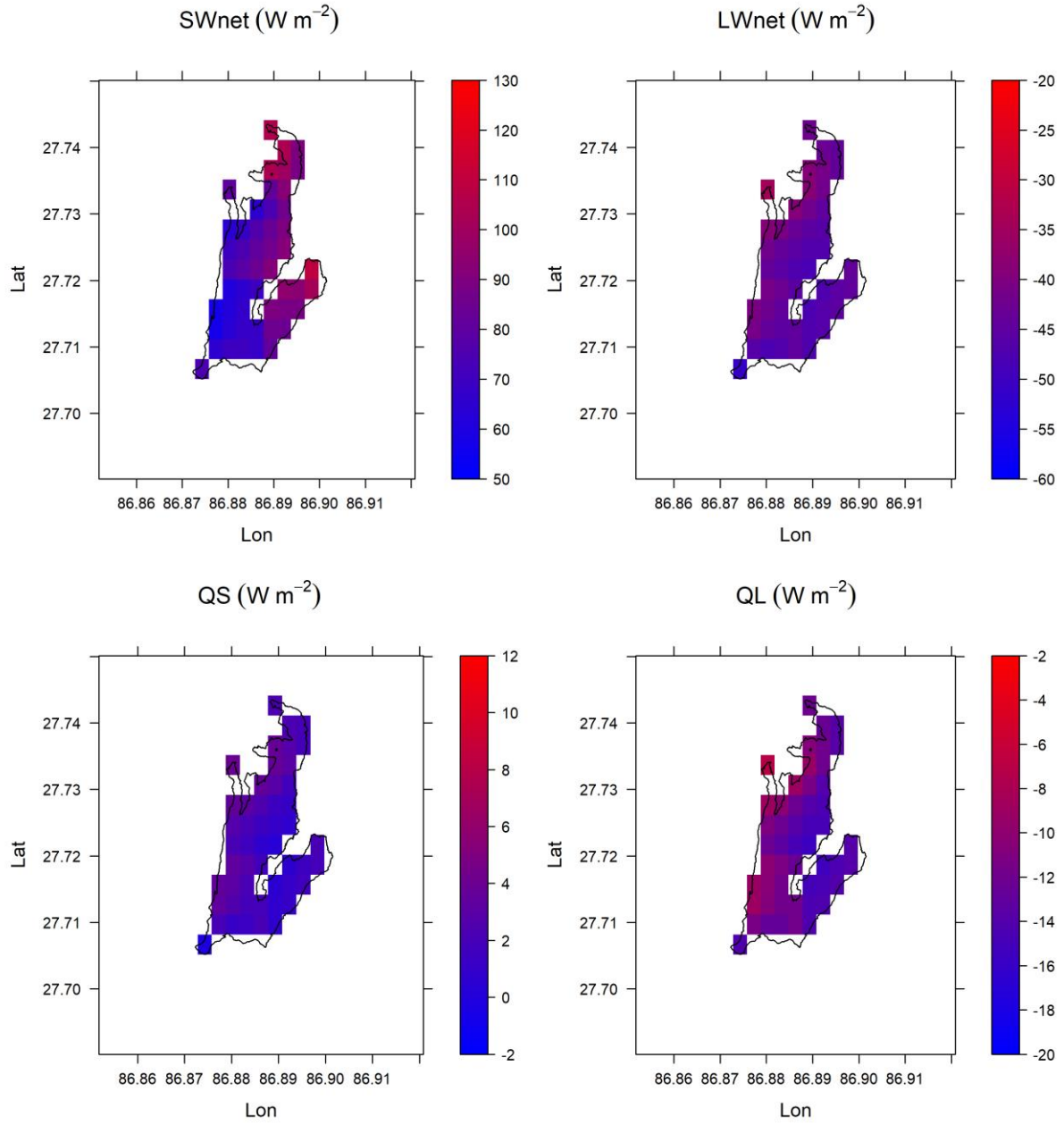


1258
 1259
 1260

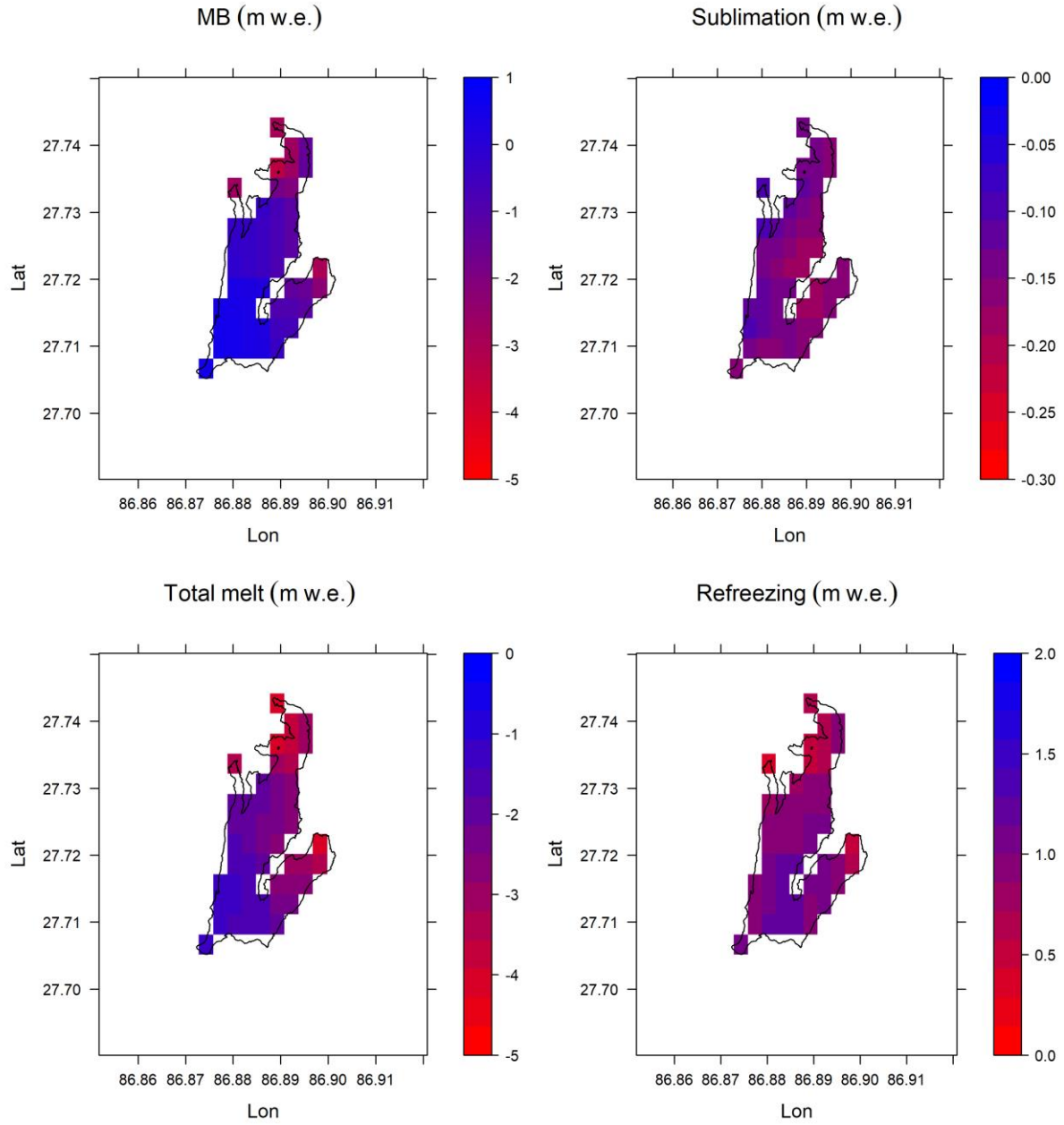
Figure S11. Same as Fig. S9 for the year 2017/18



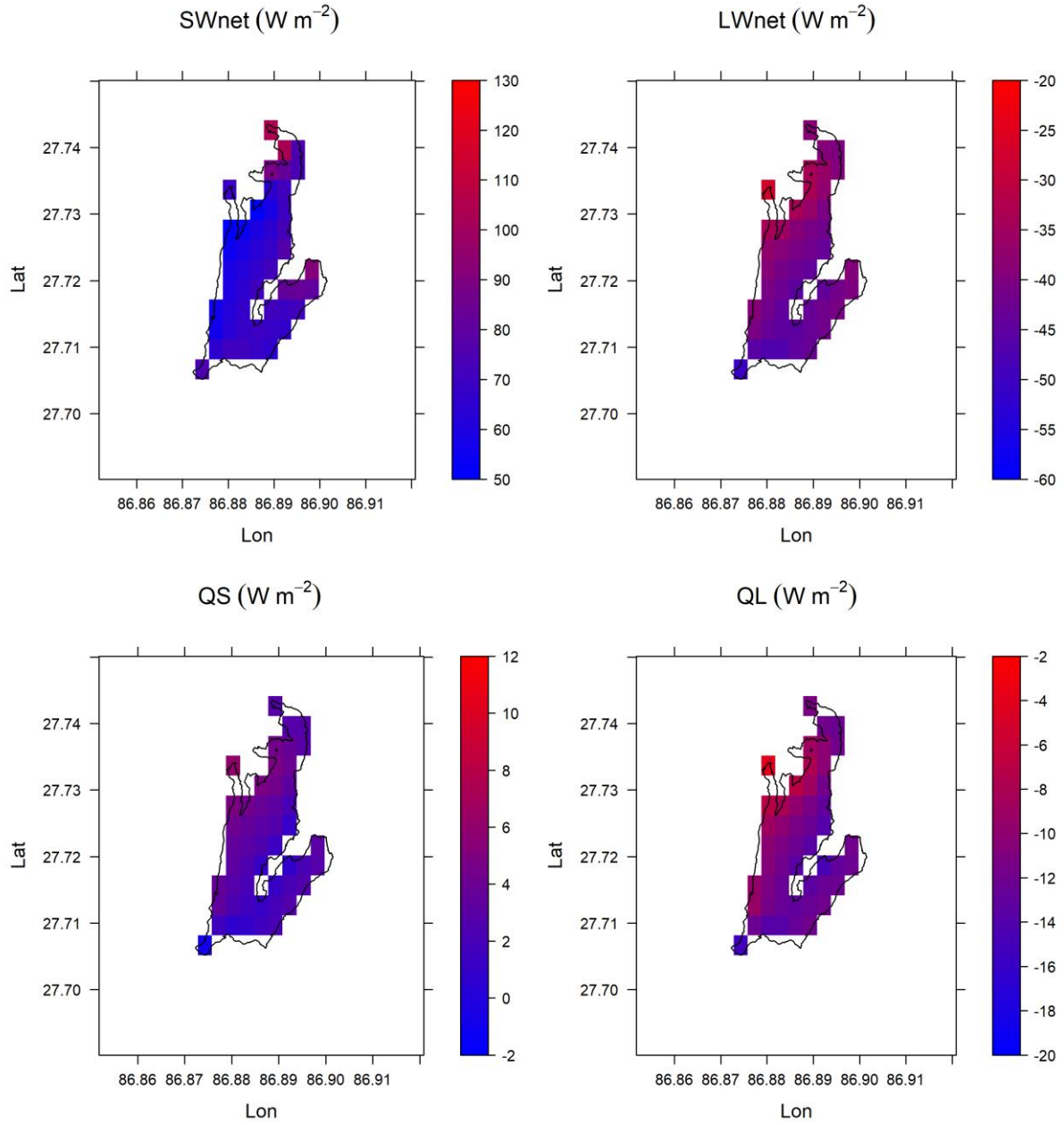
1261
 1262 *Figure S12. Same as Fig. S10 for the year 2017/18*



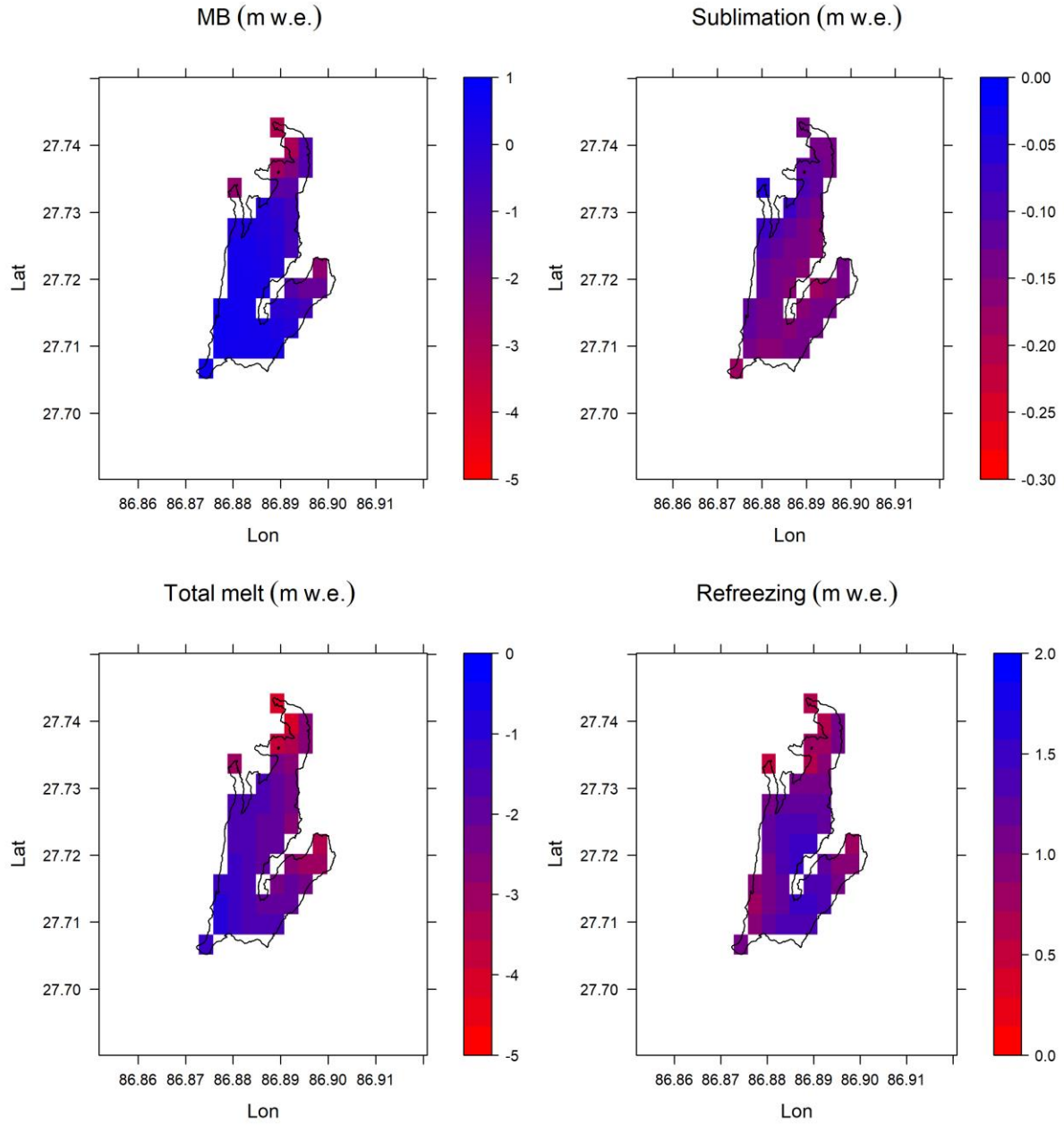
1263
 1264 *Figure S13. Same as Fig. S9 for the year 2018/19*
 1265



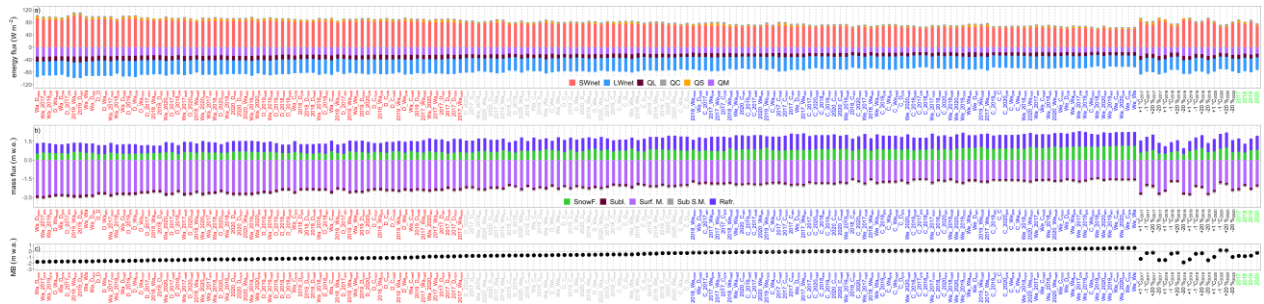
1266
 1267 *Figure S14. Same as Fig. S10 for the year 2018/19*



1268
 1269 *Figure S15. Same as Fig. S9 for the year 2019/20*

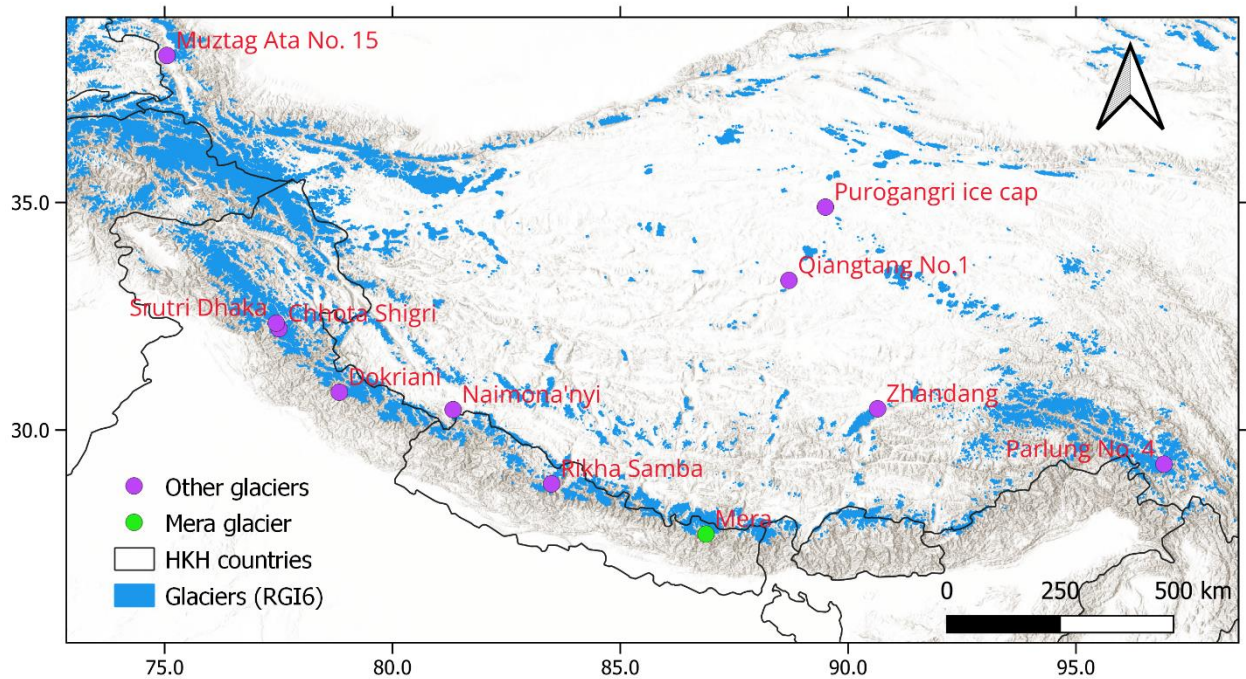


1270
 1271 *Figure S16. Same as Fig. S10 for the year 2019/20*
 1272
 1273



1274

1275 Figure S17. Glacier-wide (a) energy fluxes, (b) mass flux components, and (c) mass balance from the reference year (RY, in green
 1276 on the x-axis) as well as all classical (in black) and synthetic (in red, grey and blue) scenarios. Synthetic scenarios are sorted in
 1277 ascending order of glacier-wide mass balance, from the most negative (-1.76 m w.e.) to the most positive mass balance (0.54 m
 1278 w.e.). The colour code of synthetic scenarios visualises the mass balance range: MB < -0.80 m w.e. (red); -0.80 m w.e. ≤ MB ≤
 1279 0.25 m w.e. (grey) and -0.25 m w.e. < MB (blue). SWnet = net shortwave radiation, LWnet = net longwave radiation, QL = latent
 1280 heat flux, QS = sensible heat flux, QC = subsurface heat flux, QR = rain heat flux, QM = available melt energy at the surface,
 1281 SnowF. = solid precipitation, Subl. = sublimation, Surf. M. = melt at surface Sub S. M. = subsurface melt and Refr. = refreezing.
 1282 2017, 2018, 2019 and 2020 are the mass balance years 2016/17, 2017/18, 2018/19 and 2019/20, respectively.
 1283



1284 Figure S18. Location of glaciers where SEB studies have been conducted in HMA after 2014, and listed in Table 8.
 1285

1286
 1287
 1288 **References**

1289 Anderson EA (1976) A point energy and mass balance model of a snow cover. *Technical Report, National*
 1290 *Weather Service (NWS), United States.*

1291 Arndt A, Scherer D and Schneider C (2021) Atmosphere driven mass-balance sensitivity of Halji glacier,
 1292 Himalayas. *Atmosphere* **12**(4). doi:10.3390/ATMOS12040426.

1293 Arndt A and Schneider C (2023) Spatial pattern of glacier mass balance sensitivity to atmospheric forcing
 1294 in High Mountain Asia. *Journal of Glaciology*, 1–18. doi:10.1017/JOG.2023.46.

1295 Boone A (2002). Description du schéma de neige ISBA-ES (Explicit Snow). Centre National de Recherches
 1296 Météorologiques, Météo-France, Toulouse. Available from:
 1297 <http://www.cnrm.meteo.fr/IMG/pdf/snowdoc.pdf>.

1298 Essery R, Morin S, Lejeune Y and B Ménard C (2013) A comparison of 1701 snow models using
 1299 observations from an alpine site. *Advances in Water Resources* **55**, 131–148.

- 1300 doi:10.1016/j.advwatres.2012.07.013.
- 1301 Gurung TR, Kayastha RB, Fujita K, Joshi SP, Sinisalo A and Kirkham JD (2022) A long-term mass-balance
1302 reconstruction (1974–2021) and a decadal in situ mass-balance record (2011–2021) of Rikha Samba
1303 Glacier, central Himalaya. *Journal of Glaciology*, 1–14. doi:10.1017/JOG.2022.93.
- 1304 Oerlemans J and Knap W (1998) A 1 year record of global radiation and albedo in the ablation zone of
1305 Morteratschgletscher, Switzerland. *Journal of Glaciology* **44**(147), 231–238.
1306 doi:10.1017/S0022143000002574.
- 1307 Oulkar SN and 7 others (2022) Energy fluxes, mass balance, and climate sensitivity of the Sutri Dhaka
1308 Glacier in the western Himalaya. *Frontiers in Earth Science*, 1298. doi:10.3389/FEART.2022.949735.
- 1309 Sauter T, Arndt A and Schneider C (2020) COSIPY v1.3 – an open-source coupled snowpack and ice
1310 surface energy and mass balance model. *Geoscientific Model Development* **13**(11), 5645–5662.
1311 doi:10.5194/gmd-13-5645-2020.
- 1312 Srivastava S and Azam MF (2022) Mass- and Energy-Balance Modeling and Sublimation Losses on
1313 Dokriani Bamak and Chhota Shigri Glaciers in Himalaya Since 1979. *Frontiers in Water* **4**(April), 1–
1314 21. doi:10.3389/frwa.2022.874240.
- 1315 Sunako S, Fujita K, Sakai A and Kayastha RB (2019) Mass balance of Trambau Glacier, Rolwaling region,
1316 Nepal Himalaya: in-situ observations, long-term reconstruction and mass-balance sensitivity.
1317 *Journal of Glaciology* **65**(252), 605–616. doi:10.1017/jog.2019.37.
- 1318 Zhu M, Yang W, Yao T, Tian L, Thompson LG and Zhao H (2021) The Influence of Key Climate Variables on
1319 Mass Balance of Naimona'nyi Glacier on a North-Facing Slope in the Western Himalayas. *Journal of*
1320 *Geophysical Research: Atmospheres* **126**(7). doi:10.1029/2020JD033956.
- 1321 Zhu M, Yao T, Yang W, Xu B, Wu G and Wang X (2018) Differences in mass balance behavior for three
1322 glaciers from different climatic regions on the Tibetan Plateau. *Climate Dynamics* **50**(9–10), 3457–
1323 3484. doi:10.1007/s00382-017-3817-4.
- 1324
- 1325